

Heidar Hüttmann

COSMIC RAY MULTIPLICITY OBSERVED BY THE DOMC NEUTRON MONITOR

Study of the Ground Level Enhancement in October and the Forbush Decrease in November 2021

COSMIC RAY MULTIPLICITY OBSERVED BY THE DOMC NEUTRON MONITOR

Study of the Ground Level Enhancement in October and the Forbush Decrease in November 2021

Heidar Hüttmann
Master thesis
Spring 2024
Data Analytics and Project
Management
Oulu University of Applied Sciences

ABSTRACT

Oulu University of Applied Sciences
MSc. Data Analytics and Project Management

Author: Heidar Hüttmann

Title of thesis: Cosmic Ray Multiplicity observed by the DOMC Neutron Monitor. Study of the Ground Level Enhancement in October and the Forbush Decrease in November 2021.

Supervisors: Ilpo Virtanen (Oulu University of Applied Sciences), Stepan Poluianov (University of Oulu)

Term and year when the thesis was submitted: Spring 2024

Number of pages: 48

Through its magnetic activity and bursts of electromagnetic radiation and energetic particles, the Sun influences the flux of cosmic ray particles reaching Earth in terms of magnitude and energy spectrum. The resulting effect on space weather has practical importance for human activities in space, in the air and on the Earth's surface. In this thesis, two cosmic ray related events in the year 2021, namely a Ground Level Enhancement (GLE) and a Forbush decrease (FD), were studied based on data generated by two mini neutron monitors (NM) located at a research station in Antarctica. In particular, the distribution of waiting times, i.e. the difference between the arrival times of two subsequent counts registered by the NM, was analysed using different proxy variables aiming to reflect the energy spectrum of the incident particles. While low-energy neutrons lead to single detection events, neutrons with higher energies produce additional neutrons through interactions with the lead of the NM. This means a single incident neutron with sufficient energy (i.e. a leader count) results in multiple detection events with shorter waiting times (i.e. follower counts), which is referred to as multiplicity. The different proxy variables are based on the ratio of leader to follower counts (i.e. the leader fraction) and were compared in terms of meaningfulness and applicability for the study of GLEs and FDs. The study accounted for atmospheric pressure effects on the spectra of neutrons in air. The five main results of this thesis are:

1. The initially observed spikes in the long waiting time tail of the waiting time distribution (WTD) were found to be caused by the data acquisition system of the NM. If instead of the timestamp of the Raspberry Pi micro-computer the timestamp of the PIC32 microcontroller is used for calculating the waiting time, the spikes in the WTD disappear and the long waiting time tail follows the expected exponential shape.
2. A new method to calculate a proxy variable for the multiplicity and the energy spectrum of the incident particles was developed based on the WTD and the statistical properties of leader counts.
3. DOMB is not a perfect bare NM, as was found from the WTD analysis. The neutrons produced in the lead of DOMC can reach the neighbouring DOMB and lead to the registration of multiplicity counts.
4. The barometric correction coefficients for the DOMC NM for the total count rate, leader count rate and three different proxy variables were determined.
5. From a numerical and graphical comparison of the different proxies for the energy spectrum of incident atmospheric particles, the new proxy variable appears to better reflect the expected trends during the GLE and FD. Considering the underlying variability, however, the changes during the GLE and FD cannot be judged statistically significant.

Keywords: Cosmic rays, Multiplicity, Leader fraction, Neutron monitor, Ground Level Enhancement, Forbush decrease

ACKNOWLEDGEMENTS

The Italian Polar Program PNRA (via projects LTCPAA PNRA 2015/AC3 and BSRN PNRA OSS-06), the French Polar Institute IPEV, and the Finnish Antarctic Research Programme FINNARP are acknowledged for hosting the neutron monitors DOMC and DOMB. Gratitude is due to Sodankylä Geophysical Observatory (University of Oulu, Finland) for the access to the neutron monitor raw data and the computational software. Thanks are also due to Prof. Du Toit Strauss for sharing his insights on the neutron monitor data.

LIST OF ABBREVIATIONS

CME	<i>Coronal Mass Ejection</i>
CR	<i>Cosmic Rays</i>
DAQ	<i>Data Acquisition System</i>
FD	<i>Forbush Decrease</i>
GCR	<i>Galactic Cosmic Rays</i>
GLE	<i>Ground Level Enhancement</i>
M	<i>Multiplicity</i>
NM	<i>Neutron Monitor</i>
PIC	<i>Programmable Intelligent Computer</i>
RaspPi	<i>Single-board Computer Raspberry Pi</i>
SEP	<i>Solar Energetic Particles</i>
SD	<i>Standard Deviation</i>
UTC	<i>Coordinated Universal Time</i>
WTD	<i>Waiting Time Distribution</i>

LIST OF SYMBOLS

t_1	<i>Left Time Bin Edge</i>
t_2	<i>Right Time Bin Edge</i>
w	<i>Time Bin Width</i>
ν	<i>Count Density, i.e. Counts per Bin Width</i>
α	<i>Model Parameter, Average Rate of M1 Events</i>
A	<i>Model Parameter</i>
p	<i>Probability</i>
Δt	<i>Waiting Time</i>
τ	<i>Time Window Size</i>
ΔP	<i>Relative Pressure</i>
β	<i>Barometric Correction Coefficient</i>
C_0	<i>Uncorrected (Raw) Count Rate</i>
C	<i>Pressure-Corrected Count Rate</i>
C_{tot}	<i>Total Count Rate</i>
C_{lead}	<i>Leader Count Rate</i>
$C_{\text{lead,s}}$	<i>Leader Count Rate in the Short Waiting Time Range</i>
$C_{\text{lead,l}}$	<i>Leader Count Rate in the Long Waiting Time Range</i>
C_{M1}	<i>M1 Event Count Rate</i>
C_{follow}	<i>Follower Count Rate</i>
L_{lead}	<i>Leader Fraction</i>
L_{M1}	<i>M1 Fraction</i>
L_{NEW}	<i>NEW Leader Fraction</i>

CONTENTS

ABSTRACT	3
ACKNOWLEDGEMENTS	4
LIST OF ABBREVIATIONS	5
LIST OF SYMBOLS	6
1 INTRODUCTION	8
2 THEORETICAL BACKGROUND	10
3 MATERIALS AND METHODS	16
3.1 The instrument and data	16
3.2 Exploratory data analysis	19
3.3 Waiting time histograms	21
3.4 Spike analysis	23
3.5 Multiplicity and leader fraction	26
3.6 Atmospheric pressure correction	31
4 RESULTS AND DISCUSSION	32
4.1 Atmospheric pressure correction	32
4.2 Study of the GLE and Forbush decrease	34
5 CONCLUSIONS	41
REFERENCES	43

1 INTRODUCTION

Our planet is subject to a constant bombardment of cosmic ray (CR) particles of varying energies. Through different processes, the Sun influences the flux of CR particles reaching Earth in terms of magnitude and energy spectrum. The resulting effect on space weather has practical importance for human activities in space, in the air and on the Earth's surface. In this thesis, two cosmic ray related events in the year 2021 were studied, namely a Ground Level Enhancement (GLE) and a Forbush decrease (FD). For this purpose, data generated by neutron monitors (NM) located at a research station in Antarctica was analysed. In particular, the distribution of waiting times between counts registered by the NM was analysed using different proxy variables, which aim to reflect the energy spectrum of the incident particles. In this context, a new method to calculate such a proxy variable was developed and compared to other proxies in terms of meaningfulness and applicability for the study of the GLE and Forbush decrease. The study accounted for atmospheric pressure effects for which correction coefficients for the different variables are determined.

Note that this thesis is at the interface between space physics, i.e. the topical field, and data analytics, i.e. the degree programme. Therefore, the theoretical descriptions and physical interpretations are not provided to the same level of detail as one would expect from a physics degree thesis. Instead, they are limited to the extent necessary to give context for readers concerned with data analytics on the one, and provide value for the scientific community in the field of cosmic ray research on the other hand. In addition, the thesis points the interested reader to a number of relevant references for further information.

Chapter 2 introduces CR and a selection of processes on the Sun that influence space weather and can lead to GLEs and Forbush decreases. The interactions of CR and the Earth's atmosphere, as well as the design and operating principles of NM are described. The significance of cosmic ray research for radiation protection related to space exploration, aviation, as well as for avionics and electronic systems of critical infrastructure is also covered in Chapter 2. In Chapter 3, the DOMC and DOMB NM located in Antarctica, and the used data sets are presented. It follows an exploratory data analysis including an investigation of distinct spikes found in the waiting time distributions (WTD). Furthermore, the concept of multiplicity and leader fraction is introduced together with different proxy variables for

the energy spectrum of incident atmospheric particles. Chapter 3 finishes with the description of a new method to calculate the leader fraction. Chapter 4 presents the results for the atmospheric pressure correction and discusses them in the light of other related works. Additionally, Chapter 4 includes the results from the analysis of the GLE and Forbush decrease using different proxies for the hardness of incident atmospheric particle spectra. The conclusions are presented in Chapter 5, including a summary of the main findings, their practical implications, and a description of future research needs and possible research directions.

2 THEORETICAL BACKGROUND

Galactic cosmic rays (GCR) are omnipresent particles, mostly protons, alpha particles and heavier nuclei, from extraterrestrial sources with energies in the range of 10^6 – 10^{20} eV/nucleon, that interact with matter and magnetic fields (Aharonian et al., 2012; Bazilevskaya et al., 2014; Blanco et al., 2024). GCR are modulated by the Sun’s cyclic variations in its magnetic activity, which influences space weather and impacts Earth’s environment (Banglieng et al., 2020; Bazilevskaya et al., 2014; Jordan et al., 2011; Malandraki & Crosby, 2018). One of the manifestations of solar activity are solar flares, i.e. intense bursts of electromagnetic radiation and energetic particles (Firoz et al., 2010, 2011), that can trigger coronal mass ejections (CMEs), i.e. massive explosions of solar plasma and magnetic fields into space (Jordan et al., 2011; Kahler, 1987). Solar energetic particle (SEP) events are direct outcomes of solar flares and CMEs (Aran et al., 2018; Firoz et al., 2011; Gopalswamy et al., 2012, 2002). These involve the acceleration of particles to high energies, contributing to the influx of solar particles into the heliosphere (Aran et al., 2018; Bazilevskaya et al., 2014; Gopalswamy et al., 2012; Malandraki & Crosby, 2018).

Strong SEP events can lead to sharp and short-lasting increases in cosmic ray intensity observed on Earth, i.e. the background determined by the GCR is increased by the SEP. This is referred to as ground level enhancements (GLE) (Bazilevskaya et al., 2014; Chukwudi et al., 2022; Firoz et al., 2011; Heber et al., 2018; Malandraki & Crosby, 2018; Medina et al., 2013; Poluianov et al., 2017; Shea & Smart, 2012). Besides the increased CR flux, a GLE is characterised by a softening of the energy spectrum (Mishev et al., 2022; Papaioannou et al., 2022). This is because SEP are relatively soft compared to GCR and thus, the energy spectrum of the cosmic rays as the sum of GCR and SEP becomes softer. CME can deflect some GCR particles and cause a reduction of the cosmic ray intensity measured near or on Earth (Blanco et al., 2024; Cane et al., 1993; Jordan et al., 2011). Typically, the drop in the cosmic ray intensity is sharp and is followed by a recovery phase of several days (Jämsen et al., 2007). This phenomenon is called Forbush decrease (FD) after Forbush (1937). Forbush decreases are associated with a decrease in GCR flux and a hardened energy spectrum (Blanco et al., 2024; Miroshnichenko, 2018; Ruffolo et al., 2016), because GCR in the lower-

energy part of the spectrum are more easily deflected by the magnetic field of the CME.

The Earth's magnetic field exerts a shielding effect, barring CR with rigidities¹ below a specific threshold from accessing the atmosphere at distinct geomagnetic latitudes (Cooke et al., 1991; Gerontidou et al., 2021; Smart & Shea, 2009). This is called the geomagnetic rigidity cutoff. Trajectories of charged particles within Earth's magnetosphere are influenced by the geomagnetic field, creating specific asymptotic acceptance cones (Fig. 1) that indicate the directions from which a location on Earth receives particles with predetermined rigidities (Gerontidou et al., 2021; Poluianov et al., 2017; Rao et al., 1963). Near the Earth's magnetic poles with their vertical magnetic field lines, it is easiest for CR to enter the atmosphere of the Earth, especially if the charged particles arrive parallel to the magnetic field lines. This corresponds to a zero geomagnetic cutoff rigidity in the polar regions. The highest geomagnetic cutoff rigidities (~ 15 GV) are found near the equator (Bütikofer, 2018; Gerontidou et al., 2021; Malandraki & Crosby, 2018; Shea & Smart, 2012).

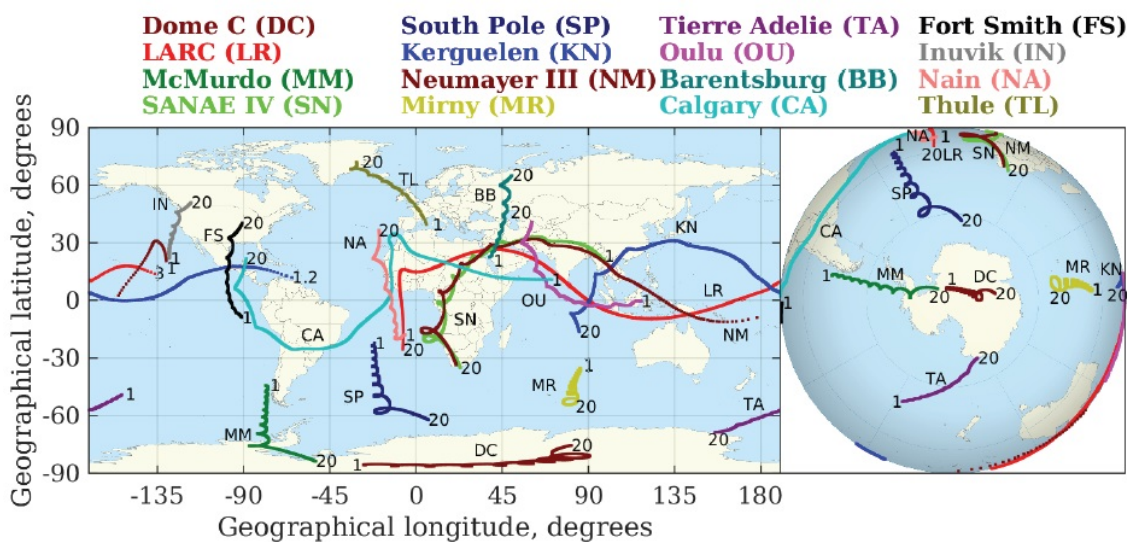


FIGURE 1. Asymptotic acceptance cones with particle rigidities in GV for different polar NM stations. Image by Poluianov et al. (2015) distributed under CC BY 3.0.

Upon entering the Earth's atmosphere, cosmic rays initiate complex interactions with atmospheric constituents. The collisions of primary cosmic ray particles with atmospheric atoms lead to cascades of reactions involving ionization, electromagnetic, and nuclear processes (Bütikofer, 2018; Shea & Smart, 2012). These reactions give rise to air showers, combining electromagnetic, muonic and hadronic components, as well as neutrinos (Fig. 2). The electromagnetic component mainly involves γ -rays, electrons and positrons, while the hadronic component encom-

¹The rigidity is a measure for the impact that Earth's magnetic field has on the trajectory of cosmic rays and depends on the particle's momentum and charge. A larger rigidity means a weaker deflection of the particle by the magnetic field (Larsen et al., 2023).

pass protons, neutrons, pions and other hadrons. The development of these showers involves processes such as particle decays, pair production, spallations, scattering interactions and energy losses, shaping the energy spectrum of secondary particles reaching the Earth's surface (Bütikofer, 2018).

In addition to the geomagnetic cutoff related to the Earth's magnetic field, the interactions of cosmic ray particles in the atmosphere contribute to a atmospheric cutoff, which is determined by the atmospheric density and hence, by the altitude (see also Section 3.6). At the geomagnetic poles, the cutoff rigidity is predominantly dependent on the atmospheric pressure (cutoff rigidity of ~ 1 GV), while at the equator the geomagnetic shielding effect dominates (cutoff rigidity of ~ 15 GV, see above) (Bütikofer, 2018; Mishev & Poluianov, 2021; Poluianov & Batalla, 2022; Ruffolo et al., 2016; Shea & Smart, 2012). While energies of the most numerous primary cosmic rays with energies below 10^{15} eV cannot be measured directly on the Earth's surface, insights on their energy spectrum can indirectly be gained through a comparison of count rates recorded by the worldwide network of approximately 50 neutron monitors (NMs) with varying cutoff rigidities due to their locations at different latitudes and altitudes (Bütikofer, 2018; Ruffolo et al., 2016).

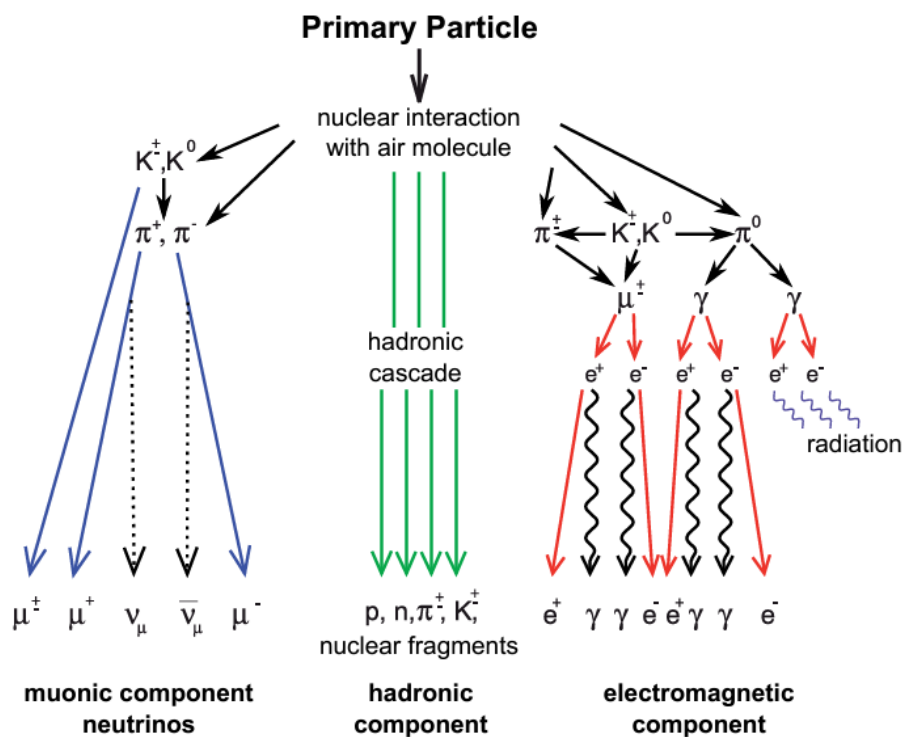


FIGURE 2. Showers of cosmic ray reactions with particles of the atmosphere. Image by Haungs et al. (2015) distributed under CC BY 3.0.

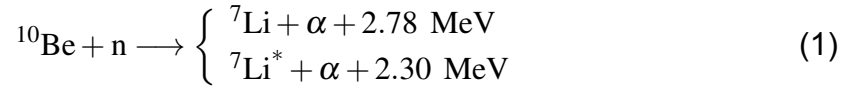
A NM is a scientific instrument designed to detect and measure secondary cosmic ray particles, predominantly neutrons and protons (approximately 90% and 6%, respectively), in the Earth's atmosphere (Bütikofer, 2018; Jämsen et al., 2007;

Mangeard et al., 2016; Ruffolo et al., 2016; Similä et al., 2021). The basic components of a standard NM (Fig. 3) typically include a lead producer, a moderator, a reflector and a counter tube (Bütikofer, 2018; Carmichael et al., 1968; Hatton, 1971; Simpson, 1957; Strauss et al., 2020). The nucleonic components of the secondary cosmic rays can interact with the lead producer of the NM in different ways depending on their energies (Balabin et al., 2011; Ruffolo et al., 2016; Strauss et al., 2020, 2022). A low-energy secondary neutron undergoes elastic scattering at the lead-nuclei and, if sufficiently moderated, lead to single detection events. The same applies to low energetic neutrons produced in the lead through interaction of low-energy secondary atmospheric protons (Strauss et al., 2020). Secondary nucleons of higher energies, through inelastic scattering with lead-nuclei, lead to the generation of multiple evaporation neutrons. This is a two-staged process involving first the excitement of the lead-nucleus through interaction with the secondary nucleon, and the subsequent deexcitation in which evaporation neutrons are emitted (Bieber et al., 2004). The number of produced evaporation neutrons through inelastic nucleon-lead interaction depends primarily on the atomic mass of the nucleus but also on the energy of the incident nucleon (Bieber et al., 2004; Bütikofer, 2018; Hughes et al., 1964). In addition to evaporation neutrons resulting from inelastic scattering, high-energy neutrons can also induce nuclear $(n,2n)$ or $(n,3n)$ reactions in the lead target, which involve the emission of 2 or 3 prompt neutrons (Balabin et al., 2011; Bütikofer, 2018). Again, if sufficiently moderated, the multiple evaporation and prompt neutrons stemming from the same nuclear reaction of a single incident secondary cosmic ray particle in the lead producer can be detected by the NM. These detection events are correlated and the source of the so-called multiplicity, i.e. the number of counts observed in a certain time interval (Bütikofer, 2018; Ruffolo et al., 2016; Strauss et al., 2022).

The moderator's role is to slow down or moderate the evaporation and prompt neutrons produced in the lead producer, increasing the probability of neutrons to interact with the gas inside the counter tube (see below) and thus, the probability of detection. Common moderator materials include paraffin wax or polyethylene (Bütikofer, 2018; Strauss et al., 2020).

The reflector, also typically made of polyethylene or paraffin wax, fulfills a twofold role. Firstly, the reflector shields against low-energy neutrons produced by high-energy atmospheric nucleons interacting with the neutron monitor's ambient material such as the detector housing. Secondly, it reflects and moderates the evaporation and prompt neutrons from the lead producer to increase the probability of detection by the counter tube (Bütikofer, 2018; Strauss et al., 2020).

The proportional counter tubes within NMs are typically filled with BF_3 or ^3He gas and operate on the principle of gas ionization. Neutrons reaching the counter tube cause the neutron capture reactions below ionizing the gas within the tube (Knoll, 2010)



or



The counter tubes are termed proportional due to the linear relationship between the amplitude of the detected electrical signals and the energy of incident neutrons. An electronic data acquisition system provides detection, recording, amplification, discrimination and counting of the electrical signals from the counter tube (Bütikofer, 2018; Strauss et al., 2020).

To account for variations in atmospheric conditions, neutron monitors include sensors to monitor environmental parameters like atmospheric pressure and temperature. This information is used to correct and calibrate the neutron measurements, see Section 3.6.

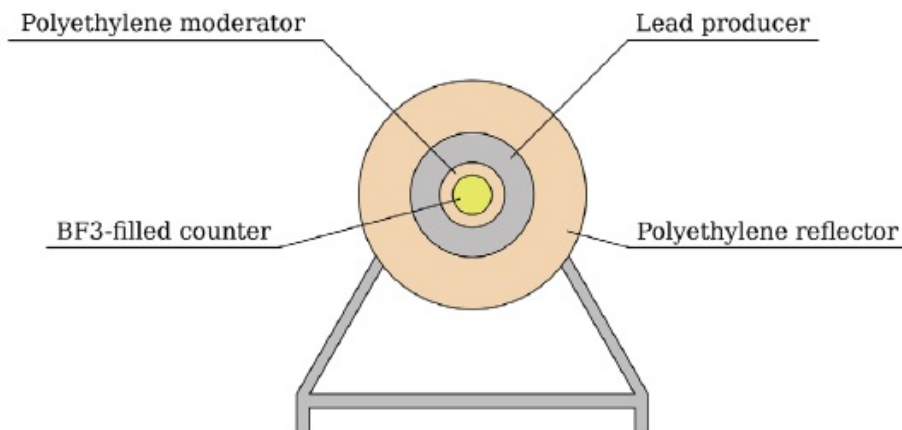


FIGURE 3. Schematic of the design of a standard mini neutron monitor. Image by Poluianov et al. (2015) distributed under CC BY 3.0.

NMs are important instruments for the study of cosmic rays. Cosmic ray research holds practical importance for modern society due to the potential risks to technology and human health associated with cosmic rays exposure. This concerns radiation protection in both space exploration and terrestrial activities at high altitudes. Events of heightened CR intensity like GLEs pose significant radiation

hazards to astronauts and space assets such as instruments, electronic components or solar arrays (Cannon et al., 2013; Jiggins et al., 2014; Malandraki & Crosby, 2018; Shea & Smart, 2012) cosmic ray research informs also legislation and radiation protection measures in the area of aviation with respect to avionics (e.g. related to disruptions in navigation and airline communication) and aircraft passengers and crew members (Beck et al., 2005; Bütikofer et al., 2008; Dyer et al., 2009, 2003, 2007; E & RolfFlückiger, 2011; Iles et al., 2004; Lantos & Fuller, 2003; Matthiä, Heber, Reitz, Meier, et al., 2009; Matthiä, Heber, Reitz, Sihver, et al., 2009).

The suggestion that systems with high safety and reliability requirements, such as those in the nuclear power industry and other critical infrastructure such as power transmission and railway systems, may need to consider increased ground level radiation on microelectronic devices underscores the broad implications and relevance of CR research (Béland & Small, 2005; Boteler, 2021; Cannon et al., 2013; Hapgood et al., 2021; Malandraki & Crosby, 2018).

3 MATERIALS AND METHODS

3.1 The instrument and data

The data analysed in this work was generated by two mini-NMs called DOMB (a "bare", lead free NM) and DOMC (a standard NM with a lead producer) situated at the French-Italian research station Concordia (Dome C) in Central Antarctica (Figs. 4 and 5). Due to its high elevation (3,233 m above sea level) and close proximity to the geomagnetic pole leading to low atmospheric and geomagnetic shielding (cutoff rigidity < 0.01 GV), respectively, the Dome C station is highly sensitive for low energy secondary particles (Poluianov et al., 2017; Strauss et al., 2020). In 2019-2020, the data acquisition system (DAQ) of DOMB and DOMC was upgraded. The DAQ system includes, among others, a Raspberry Pi 3B single-board computer and a PIC32 microcontroller with an analog-to-digital converter, which digitises the signal from the counter tube at a sampling frequency of 2 MHz, i.e. every $0.5 \mu\text{s}$ (Strauss et al., 2020). Through its interface with the PIC32, the Raspberry Pi processes and stores the raw pulse data. For a detailed description of the DAQ of the two mini-NM DOMB and DOMC, the interested reader is referred to Strauss et al. (2020).

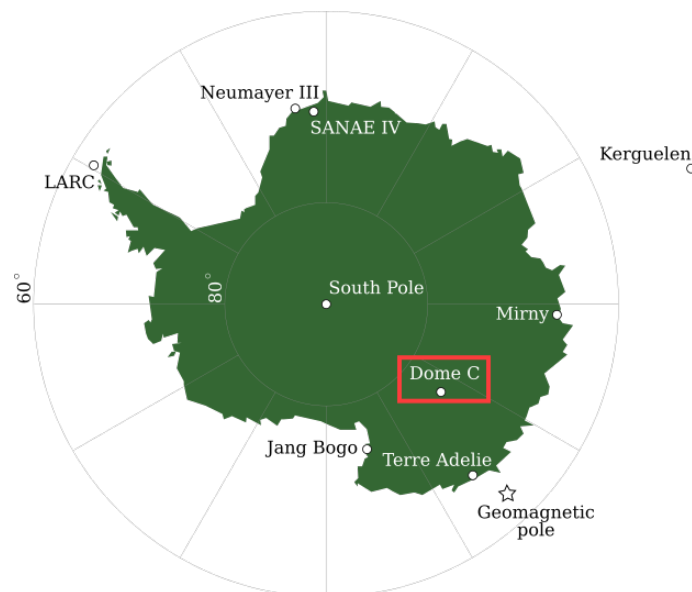


FIGURE 4. Cosmic ray stations at Antarctica including Dome C where the lead free NM DOMB and the standard NM DOMC are located. Modified image by Poluianov et al. (2015) distributed under CC BY 3.0.

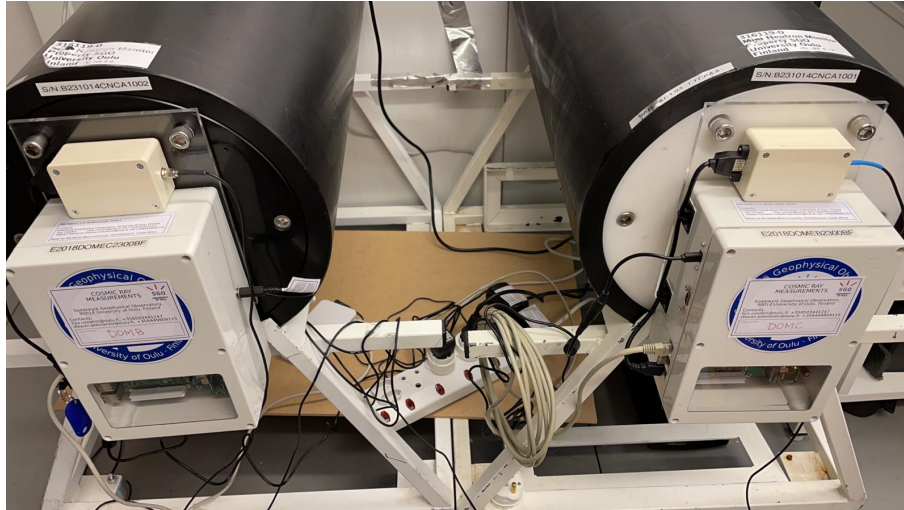


FIGURE 5. The two mini-NM called DOMB (left) and DOMC (right) located at the Concordia research station referred to as Dome C. Courtesy of Meganne Christian.

Courtesy of the Sodankylä Geophysical Observatory (University of Oulu), preprocessed data from the two mini-NM DOMB and DOMC has been made available online at <http://cosmicrays oulu.fi> since 2016. For this thesis, the raw unprocessed data was made available as comma-separated value (csv) files upon request by the thesis supervisor. Out of the several data sets produced by the NMs and associated instruments for measuring environmental conditions (Strauss & Diedericks, 2018), only two are used in this study. This is firstly the count data, which consists of

- the absolute timestamp of the Raspberry Pi (RaspPi) micro-computer broken down into minutes, seconds and microseconds,
- the relative timestamp from the rollover timer of the PIC32 microcontroller in seconds,
- the pulse amplitude in volts measured every $0.5 \mu\text{s}$,
- the pulse length in microseconds, and
- the maximum pulse amplitude in volts.

An example of the raw count data is shown in Fig. 6. The second data set used in this work contains, among others, pressure data in hPa recorded by a pressure sensor placed inside the electronics enclosure approximately every second. The data is supplemented with a timestamp of the form minutes:seconds. The data is stored in files containing the data of one-hour intervals. For this work, the DOMB and DOMC data recorded during October and November 2021 was used to study the Ground Level Enhancement (GLE) on the 28. October (referred to as GLE 73) and the Forbush decrease on the 4. November 2021.

	PIC32 timestamp	RaspPi timestamp	Pulse amplitude	Pulse length	Max. pulse amplitude
	A	B	C	D	E
1	275,3765635	59:59:976846	0.242:0.261:0.3:0.309:0.316:0.319:0.322:0.361:0.348	24	0,412
2	275,4056304	00:00:000092	0.49:1.325:1.934:2.046:2.05:1.998:1.963:1.901:1.84:	36	2,05
3	275,4091485	00:00:001990	0.222:0.235:0.267:0.28:0.258:0.258:0.235:0.229:0.22	9	0,28
4	275,4139907	00:00:035621	0.451:0.867:1.241:1.508:1.573:1.553:1.582:2.971:3.1	48	3,123
5	275,4140403	00:00:037944	0.238:0.242:0.3:0.255:0.248:0.219	6	0,3
6	275,4141664	00:00:038502	0.213:0.638:1.06:1.434:1.685:1.721:1.753:1.692:1.68	36	1,753
7	275,4143411	00:00:040231	0.593:1.018:1.254:1.334:1.328:1.308:1.289:1.254:1.1	31	1,334
8	275,4285642	00:00:041749	0.229:0.329:0.454:0.577:0.699:0.825:0.87:0.96:0.98:	35	0,98
9	275,4288666	00:00:043413	0.406:0.773:1.173:1.412:1.424:1.431:1.386:1.379:1.2	37	1,431
10	275,4716211	00:00:073704	1.183:1.753:1.853:1.853:1.84:1.801:1.756:1.714:1.64	36	1,853

FIGURE 6. Snippet of an example raw count data .csv-file. Note that the first line is a duplication of the last line of the file containing the count data of the previous hour and was discarded for the purpose of the analysis.

Note that due to instrumentation errors, the data for the following three periods (UTC) were discarded and replaced by "Not a Number" (NaN) values:

1. 7. October 00:00 – 8. October 00:00
2. 30. October 23:00 – 31. October 04:00
3. 23. November 00:00 – 1. December 00:00

The Matlab software version R2023b (The MathWorks Inc., 2023) was used for processing and analysing the data. Custom Matlab scripts and functions were developed for processing the raw data, calculating additional quantities of interests (e.g. waiting times (Section 3.3) and different measures for the leader fraction (Section 3.5)), fitting models (e.g. for the determination of barometric correction coefficients (Section 3.6)) and plotting. The format of the RaspPi timestamp and the pulse amplitudes with the colon (:) operator used as the separator required splitting and storing the individual values in *cell* arrays. The processed data was stored in *timetables* containing one month of data in minutely resolution. Timetables are a type of tables that can hold different data types, such as integers and cell arrays, and associate a time with each row. The row times were formed by reorganising the RaspPi timestamp data as *datetimes*. Timetables allow for a number of operations like accessing, aligning or combining data using the timestamped rows, which makes them a convenient choice for working with time series data. Custom properties were assigned to the timetables to store metadata used for tracking the origin of data (DOMB or DOMC, date information) or the units of the stored variables. The timetable properties can be called for example in connection with logical tests or for plotting purposes. All raw and processed data were stored on a cloud server (Microsoft OneDrive). The timetables containing the processed data were loaded into the Matlab workspace instead of needing to process the raw data every time.

During the period studied in this work, the average count rate after pressure correction (Section 3.6) of DOMB and DOMC was approximately 330 and 1300 counts per minute, respectively. Fig. 7 shows the pressure-corrected count rate for DOMB and DOMC data of October and November 2021, which is discussed in Chapter 4.

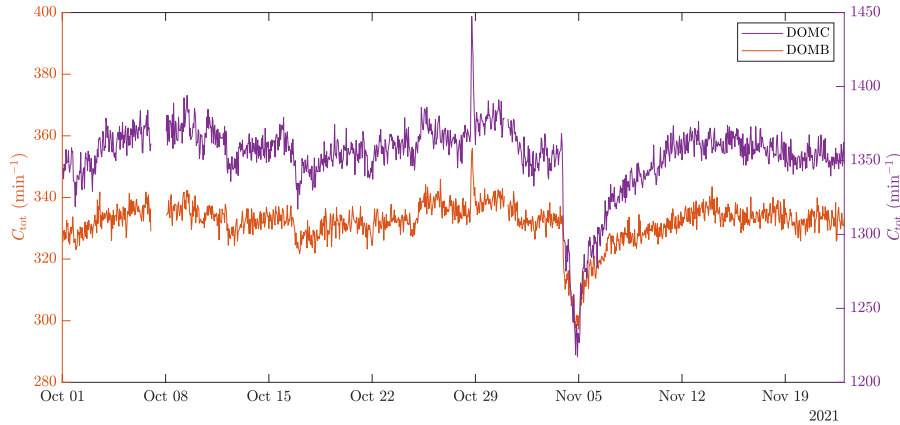


FIGURE 7. Time series of the hourly averaged total count rate C_{tot} after atmospheric pressure correction for DOMB and DOMC data from October and November 2021.

3.2 Exploratory data analysis

The relation between the pulse length and maximum amplitude is presented in the 2D-histograms in Figs. 8 and 9 for DOMC and DOMB data from October 2021, respectively. The distribution is very similar to those presented by Similä et al. (2021) for DOMC data from January to May 2020 and DOMB data from August to October 2019, or by Strauss et al. (2020) for another NM placed in Antarctica.

Similar to Strauss et al. (2020) and (Similä et al., 2021), a simple approach was used to separate the 2D-histograms into different regions A, B and C depending on different distinct pulse types observed in the data. Note that in the future, more sophisticated approaches based on clustering algorithms can be explored for separating the pulses based on their shapes.

With regard to DOMC data (Fig. 10), region A contains 76% of approximately 74.6 million counts with maximum amplitudes between 0.5 and 2.75 V and pulse lengths between 5 and 25 μs , with mean maximum amplitudes and lengths of 1.4 V and 16.4 μs , respectively. The counts in region A consist of single pulses with a step increase in amplitude (maximum reached after less than 4 μs), and a relatively slowly decline until the signal falls below the threshold of 0.2 V. The

pulses in Region A are considered to be normal pulses corresponding to incoming particles.

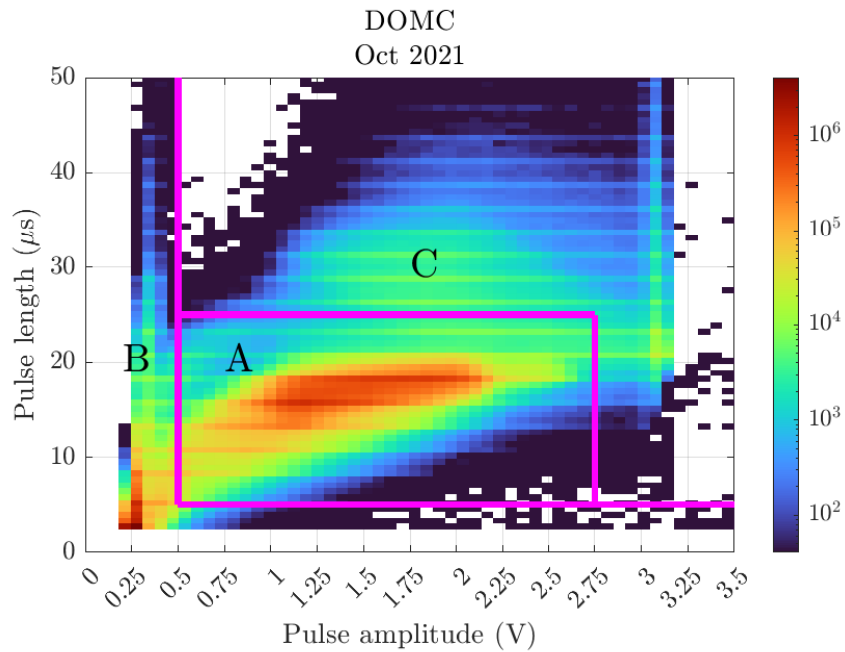


FIGURE 8. 2D-histogram of pulse length and maximum pulse amplitude for DOMC data from October 2021. The pink lines separate the data set into three regions A, B and C with distinct pulse profiles shown in Fig. 10. Regions A, B and C contain 76%, 22% and 2% of the data, respectively. The total number of data points is 74,599,494.

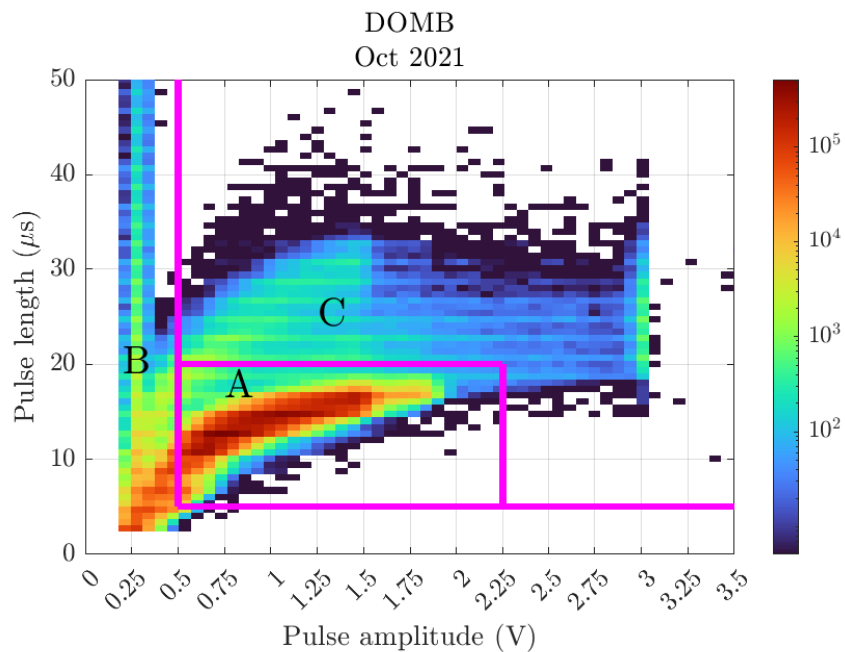


FIGURE 9. 2D-histogram of pulse length and maximum pulse amplitude for DOMB data from October 2021. The pink lines separate the data set into three regions A, B and C with distinct pulse profiles. Regions A, B and C contain 88%, 11% and <1% of the data, respectively. The total number of data points is 15,941,356.

The low (< 0.5 V) amplitude pulses of different lengths falling into region B contribute to 22% of the counts. These pulses do not display any particular shape and can be ascribed to electronic noise (Similä et al., 2021).

Pulses in region C account for 2% of the data points and are characterized by mostly double and sometimes triple or more pulses. With regard to their shape, the pulses in region C and A are similar, that is, they increase sharply and then the signal falls relatively slowly. In case of region C, however, subpulses are formed during the decay of a preceding pulse when the signal increases steeply again and reaches another maximum before decaying slowly below the instrument's threshold. Considering that succeeding pulses start at different background values, the amplitudes of individual subpulses is of comparable size, which is consistent with the study of Similä et al. (2021). According to Similä et al. (2021), these multiple pulses originate from secondary nucleons of the same atmospheric cascade where the time separations between the secondary nucleons is shorter than the length of single pulses. As a result, the partially overlapping pulses are registered by the NM as single ones with longer total lengths.

The thresholds used to separate the DOMB data are slightly different than for DOMC data (cf. Figs. 8 and 9), such that region C is increased at the expense of region A. In case of DOMB data, the regions A, B and C contain approximately 88%, 11%, and $<1\%$ of the data, respectively. Despite the tighter bounds for region A, more counts fall into it when compared to DOMC data (76%).

For the remainder of this work, the noisy data (region B) and the negligible amount of overlapping pulses (region C) was discarded and only the data associated with the normal pulses of region A was used.

3.3 Waiting time histograms

The time between two subsequent pulses observed by a NM is called waiting time (Similä et al., 2021; Strauss et al., 2020, 2022; Wheatland, 2003; Wheatland & Litvinenko, 2002), time-delay (Banglieng et al., 2020; Bieber et al., 2004; Chaiwongkhot et al., 2021; Mangeard et al., 2016; Muangha et al., 2021; Ruffolo et al., 2011, 2016; Yakum et al., 2021) or interval time (Balabin et al., 2011). Strauss et al. (2020) defines the waiting time as the difference in time between the offset of one pulse, i.e. when the signal falls below the instrument's threshold, and the onset of the following pulse, i.e. when the signal exceeds the threshold again. According to Similä et al. (2021), on the other hand, the waiting time is taken as

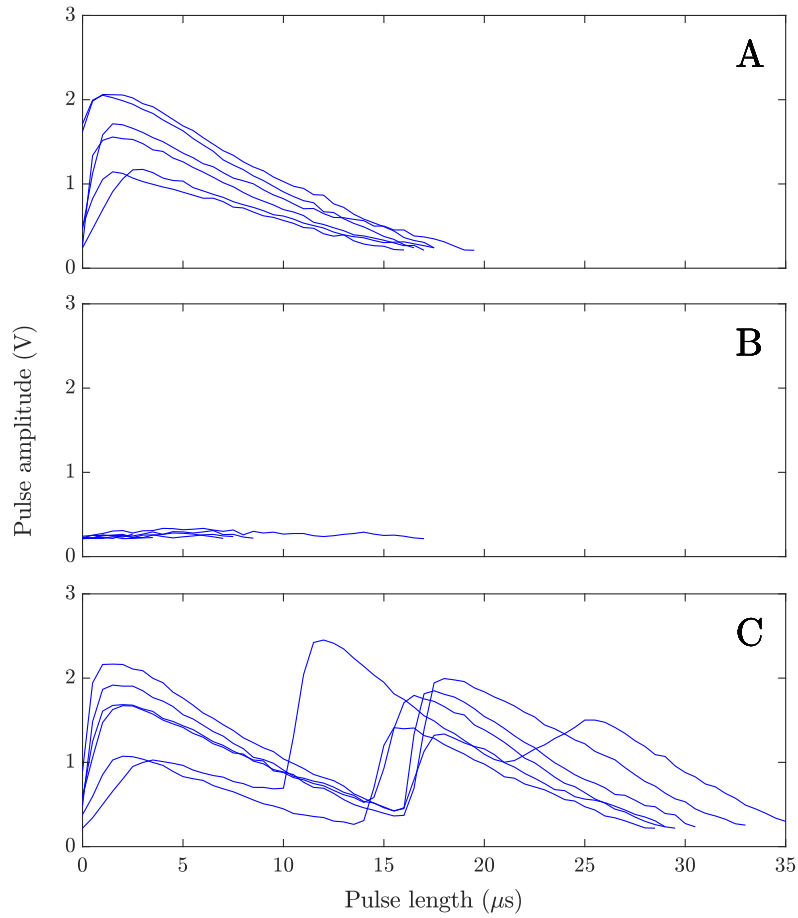


FIGURE 10. Typical profiles of pulses from the three different regions *A*, *B* and *C* shown in Fig. 8. *A*: $0.5 \text{ V} < \text{amplitude} < 2.75 \text{ V}$ & $5 \mu\text{s} < \text{length} < 25 \mu\text{s}$. *B*: $\text{amplitude} < 0.5 \text{ V}$ or $\text{length} < 5 \mu\text{s}$. *C*: $\text{amplitude} > 0.5 \text{ V}$ & $\text{length} > 25 \mu\text{s}$ or $\text{amplitude} > 2.75 \text{ V}$ & $5 \mu\text{s} < \text{length} < 25 \mu\text{s}$.

the time difference between the onsets of two subsequent pulses. This approach disregards the pulse lengths and hence, leads to an overlap of the distribution of the pulse lengths and the waiting time distribution for waiting times shorter than the pulse lengths (16.4 μs on average for the data analysed in this work, see Section 3.2). However, basing the definition of the waiting time on the onsets of two subsequent pulses is consistent with the that of a Poisson process, which can be used to describe the arrival times of random independent events of the same underlying process. Section 3.5 expands on how this can be applied to the long waiting time tail of the WTD.

In this work, the approach by Similä et al. (2021) was followed, that is, the waiting time is defined as the time between the onset of subsequent pulses, which can be directly obtained from the timestamps of individual pulses. Using the timestamp of the Raspberry Pi (RaspPi) micro-computer to calculate the waiting time, the waiting time distribution (WTD) can be arranged in logarithmically binned his-

tograms, as shown in Fig. 11 (left) for both DOMB and DOMC data from October 2021. Note that the vertical axis shows the count density, that is, the number of counts per bin width. For both DOMB and DOMC data, WTDs are bimodal, with a separation of short and long waiting times at approximately $10^4 \mu\text{s}$. When comparing the two, the WTD for DOMB data is slightly shifted towards longer waiting times. This leads to higher count densities for DOMB for waiting times in the order of magnitude $10^5 \mu\text{s}$. For shorter waiting times, the count density for DOMC exceeds that of DOMB. Of particular note are the spikes both WTDs display in the long waiting time tail, which do not appear in the works by Wheatland (2003), Bieber et al. (2004), Balabin et al. (2011), Strauss et al. (2020, 2022), Ruffolo et al. (2011, 2016), Muangha et al. (2021), Mangeard et al. (2016) and Yakum et al. (2021). Note that the long waiting time tails of the WTD for DOMB and DOMC data in Similä et al. (2021) do show some spikes, however, not to the same extent as shown in Fig. 11 (left). For the purpose of a better visualisation, Fig. 11 (right) shows the overlay of the log-log histogram of count density with the semi-log histogram of the number of counts, while keeping the logarithmic binning of the waiting times. The spikes are investigated at the example of the DOMC data in the following section.

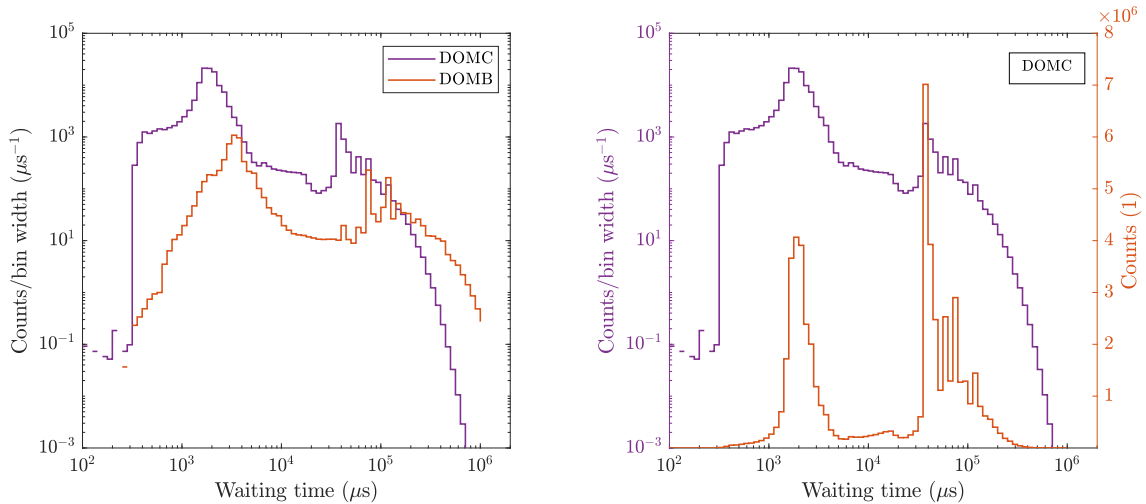


FIGURE 11. Left: Waiting time distributions for RaspPi DOMC and DOMB data from October 2021. Right: Waiting time distributions based on count density and counts for RaspPi DOMC data from October 2021. The five highest bins with long ($>10^4 \mu\text{s}$) waiting times contain approximately 33% of the data.

3.4 Spike analysis

In this section, the notable spikes in the long waiting time tail of the WTD in Fig. 11 is analysed based on the example of DOMC data for October 2021. In order to

investigate possible differences in the underlying data structure, the data falling into the five highest bins in the long ($>10^4$ μs) waiting time tail of the WTD was separated from the rest. The resulting data set associated with the spikes contains approximately one third of the data points. The pulses belonging to the two data sets, i.e. the spike data and all other data, was analysed in terms of pulse length and maximum amplitude. Table 1 shows the mean and standard deviation of these two variables for the two data sets. Except for the slightly smaller standard deviation of the pulse length in case of the spike data, the two data sets are similar in terms of the pulse shapes.

TABLE 1. Mean and standard deviation (SD) of pulse length and maximum pulse amplitude for the data points associated with the long waiting time spikes of the WTD shown in Fig. 11 and all other data.

	Spikes	All other data
Mean pulse length (μs)	16.9	16.2
SD pulse length (μs)	1.9	2.6
Mean max. amplitude (V)	1.4	1.4
SD max. amplitude (V)	0.4	0.4

This is also apparent from the 2D-histograms in Fig. 12, which display the same structure as Fig. 8 for the joint set of DOMC data from October 2021. The similarity of the data associated with the spikes in the long waiting time tail of the WTD and the remaining data in terms of pulse length and pulse amplitude is further confirmed by the overlaid histograms in Fig. 13. Therefore, it is concluded that the pulses belonging to the spikes in the long waiting time tail of the WTD do not differ from the rest of the data.

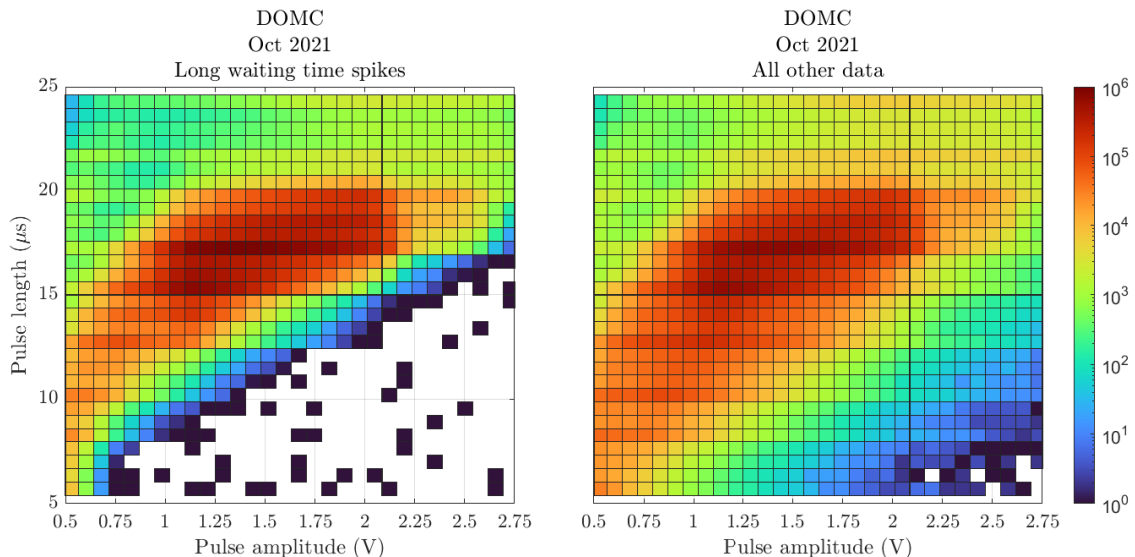


FIGURE 12. 2D-histograms of pulse length and maximum pulse amplitude for data in the five highest bins with long ($>10^4$ μs) waiting times shown in Fig. 11 (left) and the remaining data (right).

After personal communication with Prof. Strauss (2024), the cause for the dissimilarity of the WTD in Fig. 11 and other works was found to lie with the raw

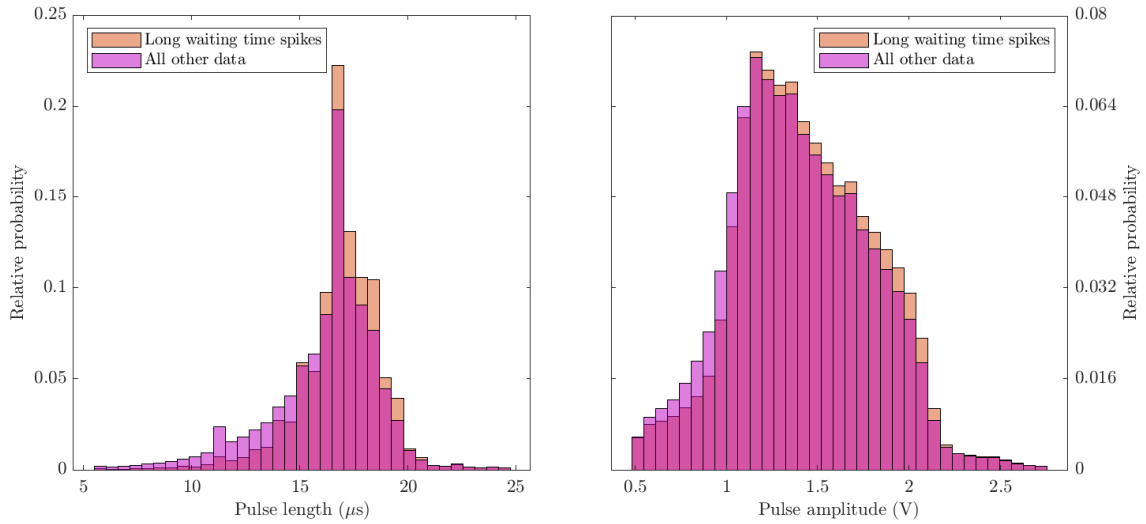


FIGURE 13. Normalised histograms (i.e. the number of elements in each bin relative to the total number of elements) of pulse length (top) and maximum pulse amplitude (bottom) for data in the five highest bins with long ($>10^4 \mu\text{s}$) waiting times shown in Fig. 11 and the remaining data.

data from the DAQ of the DOMB and DOMC NMs. If instead of the absolute timestamp of the Raspberry Pi micro-computer the relative timestamp of the PIC32 microcontroller is used for calculating the waiting time between subsequent pulses, the spikes in the long waiting time tail of the WTD disappear, as shown on the left and right of Fig. 14 for DOMC and DOMB data, respectively. This constitutes the first main finding of this thesis.

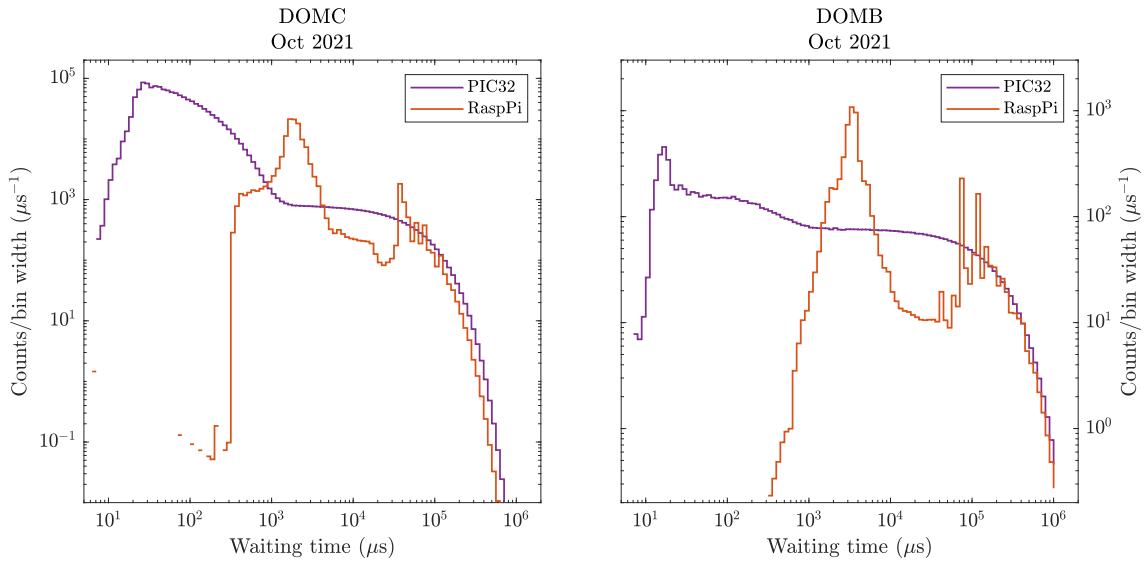


FIGURE 14. Waiting time distributions calculated from PIC32 and RaspPi timestamps from DOMC (left) and DOMB (right) data from October 2021.

The histogram of counts in Fig. 15 shows a clear bimodal distribution of waiting times with one population of short waiting times and another population of long waiting times, separated at approximately $2,000 \mu\text{s}$. Note that "(1)" is used to denote dimensionless quantities. In Section 3.5, it is described how these two populations are attributed to two different kinds of counts, namely follower and

leader counts. Also in Section 3.5, the count density histogram with the exponential tail at long waiting times is used for developing a new method to calculate the leader fraction.

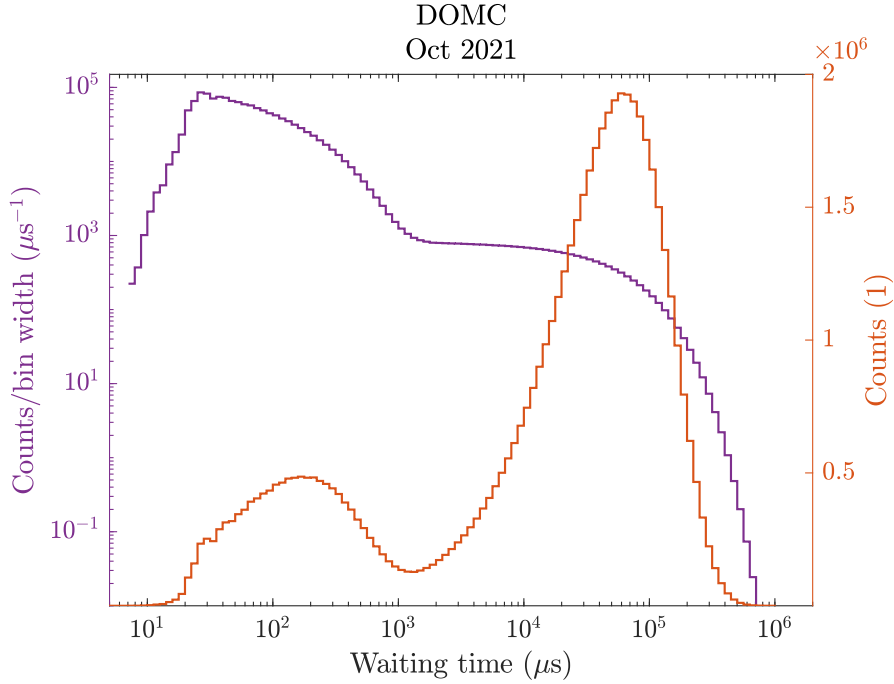


FIGURE 15. Waiting time distribution based on count density and counts for PIC32 DOMC data from October 2021 for comparison with Fig. 11 (right).

3.5 Multiplicity and leader fraction

As described in Chapter 2, secondary cosmic ray particles produced in the Earth’s atmosphere can reach ground level and, depending on their energy, undergo different types of interactions in the lead producer before being detected by a NM. The waiting time, introduced in Section 3.3, is the difference between the arrival times of two subsequent detection events, that is, between the onsets of two subsequent pulses registered by a NM. Evaporation and prompt neutrons stemming from the same nuclear reaction of a single incident secondary cosmic ray particle in the lead producer lead to clusters of correlated count events. The number of counts in a cluster detected in given time window of size τ is called multiplicity. The first count of such a cluster of counts is called leader count, while the others are called follower counts (Ruffolo et al., 2016). Low energy secondary nucleons, which undergo only elastic scattering in the lead producer are registered as single uncorrelated detection events that occur in a random fashion (Bieber et al., 2004; Ruffolo et al., 2016; Strauss et al., 2022), or in other words, as multiplicity-1 (M1) events consisting of leader counts only. This concept is visualised in Fig. 16.

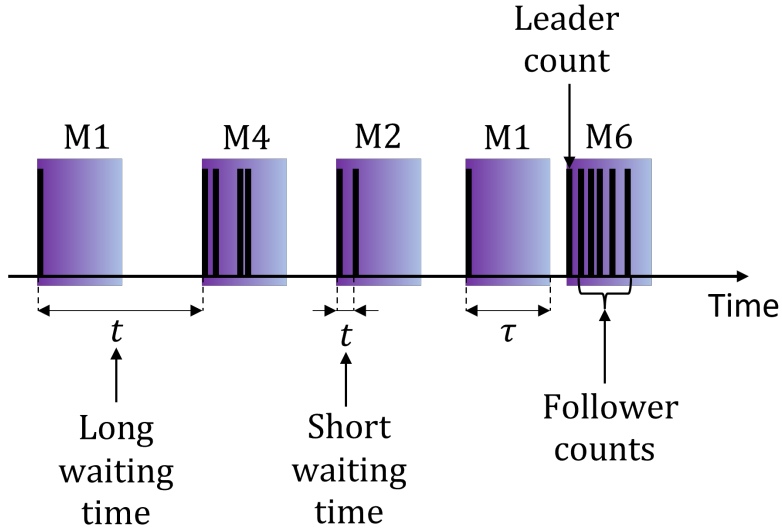


FIGURE 16. Illustration of the concept of multiplicity.

The waiting time between M1 events is larger than that for counts belonging to $M > 1$ events (Bieber et al., 2004; Mangeard et al., 2016; Strauss et al., 2020, 2022). As the M1 events occur randomly and independent from each other, their arrival times are Poisson distributed (Balabin et al., 2011; Bieber et al., 2004; Ruffolo et al., 2016; Strauss et al., 2020; Wheatland & Litvinenko, 2002)

$$p(t) = Ae^{-\alpha t}, \quad (3)$$

where $p(t)$ is the probability of observing a waiting time t between two subsequent M1 events, and A and α are model parameters related to each other through

$$\alpha = \frac{1}{A}. \quad (4)$$

In the context of a Poisson distribution, the parameter α is interpreted as the average rate at which M1 events occur.

Yakum et al. (2021) indicate a deviation of the exponential model for waiting times below 5 ms, while the data analysed by Bieber et al. (2004) showed a changeover at 4 ms, Ruffolo et al. (2016) and Balabin et al. (2011) found this to happen at 2 ms, and Ruffolo et al. (2011) and Strauss et al. (2022) reported that the exponential model is suitable for waiting times above 1 ms.

Based on the WTD for DOMC data presented in Fig. 15, a value of 2 ms (i.e. 2,000 μ s) was chosen for separating long and short waiting times, and therefore, between M1 events and events of multiplicity $M > 1$. However, it should be noted that, according to the distribution given by Equation 3, a small amount of counts in the short waiting time range is also caused by M1 events (see also Fig. 18). Using 2 ms as the value for defining the size of a time window τ , the clusters of

counts falling into it were studied for DOMC data from October and November 2021. The results are presented in Fig. 17, which shows an approximately exponential distribution of clusters of different multiplicities. In addition, every count in the analysed data was identified as either a leader or a follower count using the same time window τ . Based on this, the leader fraction L_{lead} can be calculated as the ratio of leader counts C_{lead} to the total number of counts C_{tot} (i.e. the sum of leader and follower counts)

$$L_{\text{lead}} = \frac{C_{\text{lead}}}{C_{\text{tot}}}. \quad (5)$$

The M1 fraction L_{M1} is defined as the number of multiplicity M1 events C_{M1} , divided by the number of leader counts C_{lead} (i.e. the number of clusters)

$$L_{M1} = \frac{C_{M1}}{C_{\text{lead}}}. \quad (6)$$

Due to the dependency of the number of multiplicity events on the energy of secondary particles (Chapter 2), the leader count rate and therefore the leader fraction and M1 fraction are expected to negatively correlate with the energy of secondary particles (Mangeard et al., 2016).

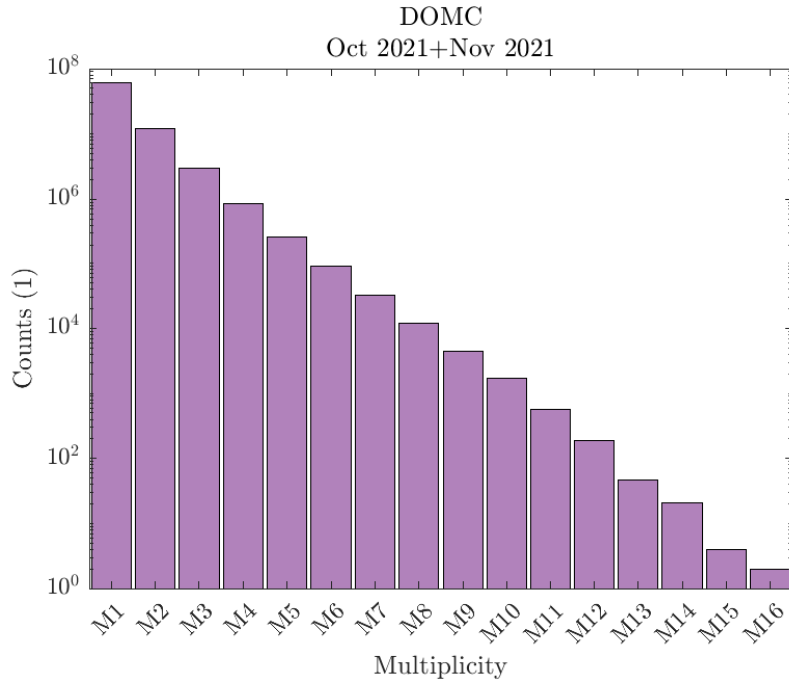


FIGURE 17. Histogram of multiplicity clusters for DOMC data from October and November 2021.

The above discussion relating to the Poisson distributed M1 counts motivated the development of a new method to calculate the leader fraction. Similar to Ruffolo

et al. (2016), Yakum et al. (2021) and Strauss et al. (2020), the method developed in this thesis involves fitting an exponential model $y(t) = Ae^{-\alpha t}$, where $y(t)$ is used to distinguish the count density of the WTD from the probability $p(t)$ in Equation 3), to the long (> 2 ms) waiting time tail of WTD for NM count data of a given time period (one hour in this work). Note that for fitting purposes, a linear regression of the natural log of the count density on the bin centers of the WTD was performed based on a linear model of the form $y(t) = b_0 + b_1 t$. Then, the parameters of the exponential model can be obtained as $A = e^{b_0}$ and $\alpha = -b_1$. The novelty of the approach presented in this thesis is that the leader fraction is obtained from the ratios of areas under the WTD demarcated by the exponential model. The new method is illustrated in Fig. 18.

The number of leader counts with waiting times > 2 ms, denoted as $C_{\text{lead,l}}$, is directly obtained from summing up the bin heights multiplied by their respective bin widths (Equation 9). In the short (< 2 ms) waiting time range, where the WTD deviates from the exponential distribution, leader counts contribute only marginally and follower counts dominate. The number of leader counts in the short waiting time range $C_{\text{lead,s}}$ is given by the exponential model $y(t) = Ae^{-\alpha t}$ or, in case the bin height is lower than predicted by the exponential model, obtained directly from the bin data (Equation 8). The remaining counts are follower counts. Summing up the leader counts in the short and the long waiting time range ($C_{\text{lead,s}}$ and $C_{\text{lead,l}}$, respectively), and dividing by the total number of counts C_{tot} , results in a value for the new leader fraction

$$L_{\text{NEW}} = \frac{C_{\text{lead,s}} + C_{\text{lead,l}}}{C_{\text{tot}}}, \quad (7)$$

where

$$C_{\text{lead,s}} = \begin{cases} \sum_i \int_{t_{1,i}}^{t_{2,i}} y(t) dt, & \text{if } v_i > y(t_{1,i}) \\ \sum_i v_i w_i, & \text{if } v_i < y(t_{1,i}) \end{cases} \quad (8)$$

and

$$C_{\text{lead,l}} = \sum_i v_i w_i, \quad (9)$$

with $t_{1,i}$, $t_{2,i}$, v_i and w_i being the left edge, right edge, count density and width of time bin i , respectively. The new method for calculating the leader fraction is the second main result of this thesis.

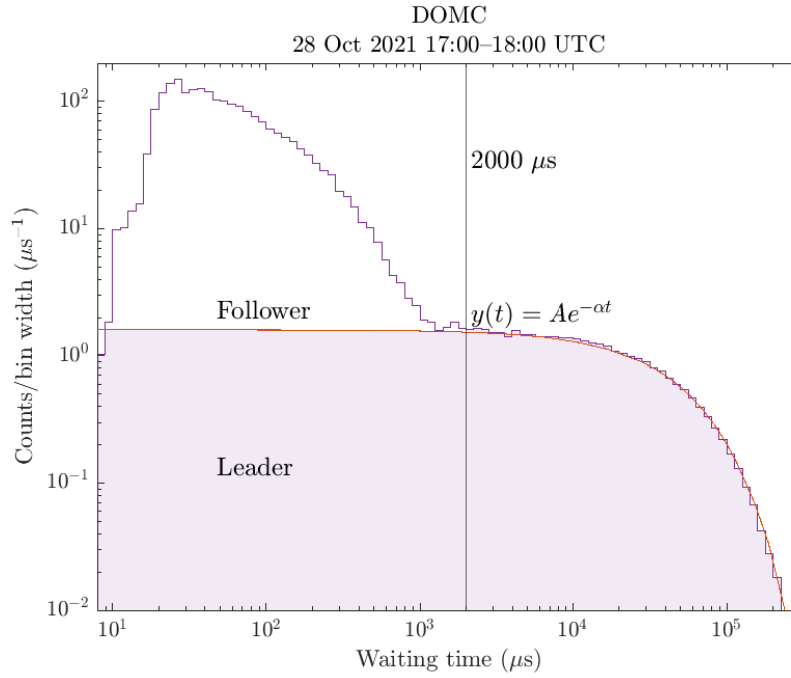


FIGURE 18. Illustration of the new method for calculating the leader fraction from area ratios of the waiting time distribution for DOMC data recorded during 17:00–18:00 UTC on the 28. October 2021. The black vertical line at 2,000 μs separates short and long waiting times. The exponential model for leader counts fitted to the long waiting time data is shown in orange.

The total and leader count rates, leader fraction, M1 fraction and the leader fraction obtained by the new method were calculated for one hour intervals of DOMC data and used to study the GLE and Forbush decrease in October and November 2021, respectively. This allows for a comparison of proxies for the multiplicity and the spectral index of the incident atmospheric particles obtained from counting pulses falling into a time window $\tau = 2$ ms, i.e. the leader fraction and M1 fraction, and a proxy directly obtained from the WTD, i.e. the new leader fraction (see Section 4.2). Before, the data needs to be corrected for atmospheric pressure effects as described in the following Section 3.6.

Interestingly, although DOMB is a bare NM without a lead producer and thus, should theoretically record only M1 events, a non-exponential excess of counts in the short waiting time range can be observed in Fig 14. Although less pronounced than for DOMC data (Fig. 18), this deviation of the WTD for DOMB data from an exponential distribution is not negligible. A possible cause lies in the proximity of the two NM of less than one meter. It can be assumed that the multiplicity counts registered by DOMB originate from neutrons produced in the lead producer of DOMC that are not effectively reflected by the reflector towards the counter tube of DOMC. The neutrons escaping DOMC can reach the neighbouring DOMB and lead to the registration of $M > 1$ events. Possible solutions to this issue are an increased thickness of the reflector material in DOMC, and a greater spacing between the two NM. This constitutes the third main finding of this thesis.

3.6 Atmospheric pressure correction

Due to the interactions of primary and secondary cosmic ray particles with the Earth's atmosphere (Chapter 2), the count rate registered by a NM on the Earth's surface depends on meteorological conditions, mainly in terms of atmospheric pressure, and to lesser extent in terms of temperature and humidity (Bütikofer, 2018). From the top of the Earth's atmosphere, the number of secondary nucleons (protons and neutrons) generated in cosmic ray showers initially increases until reaching a maximum flux at the altitude of approximately 20 km (depending on rigidity and solar activity), called the Regener-Pfotzer maximum. At lower altitudes the attenuation due to energy losses related to various interactions between secondary particles and the air dominates over the generation of secondary particles, leading to a decrease in the secondary particle flux. The attenuation is related to the amount of air passed and increases with the air density and thus, with the atmospheric pressure (Bazilevskaya et al., 2000). This forms the barometric effect, i.e., the inverse correlation of the NM count rate and atmospheric pressure.

Due to its significant effect upon the energy spectrum and the NM count rate, it is essential to accurately measure the atmospheric pressure and correct the NM data accordingly (Bütikofer, 2018). The pressure-corrected count rate C is obtained from the exponential relationship (Bütikofer, 2018)

$$C = C_0 e^{\beta \Delta P}, \quad (10)$$

where C_0 is the uncorrected (raw) count rate, β is the barometric correction coefficient and ΔP is the relative pressure, i.e. the difference between the reference pressure of 640 mbar and the measured pressure.

The raw count rate C_0 and the pressure difference ΔP were averaged over one hour intervals of periods with quiet solar conditions. For this purpose, data related to the periods of the GLE (28. October 00:00 – 29. October 00:00 UTC) and the Forbush decrease (1. November 00:00 – 12. November 00:00 UTC) were left out when determining the barometric correction coefficient. In practise, the natural log of the uncorrected count rate C_0 was taken and then β is the slope coefficient obtained from a linear regression of $\ln(C_0)$ on the pressure difference ΔP . The approach for pressure correction was applied to the total count rate C_{tot} , leader count rate C_{lead} , leader fraction L_{lead} , M1 fraction L_{M1} and the new leader fraction L_{NEW} . The results are presented in Section 4.1.

4 RESULTS AND DISCUSSION

4.1 Atmospheric pressure correction

As described in Section 3.6, the barometric correction coefficient β is obtained by a linear regression of the natural log of the variable in question on the pressure difference ΔP . For a better interpretability, the y-axis values are also given on a linear scale. The left and right of Fig. 19 show the outcome for the total count rate C_{tot} and the leader count rate C_{lead} , respectively. The barometric correction coefficient for the total count rate C_{tot} was calculated to $0.000788 \text{ hPa}^{-1}$, which is consistent with that for DOMC reported by Poluianov et al. (2015) and other NMs (Bütikofer, 2018; Ruffolo et al., 2016; Strauss et al., 2020). The barometric correction coefficient for C_{lead} of $0.000756 \text{ hPa}^{-1}$ was found to be close to that of C_{tot} .

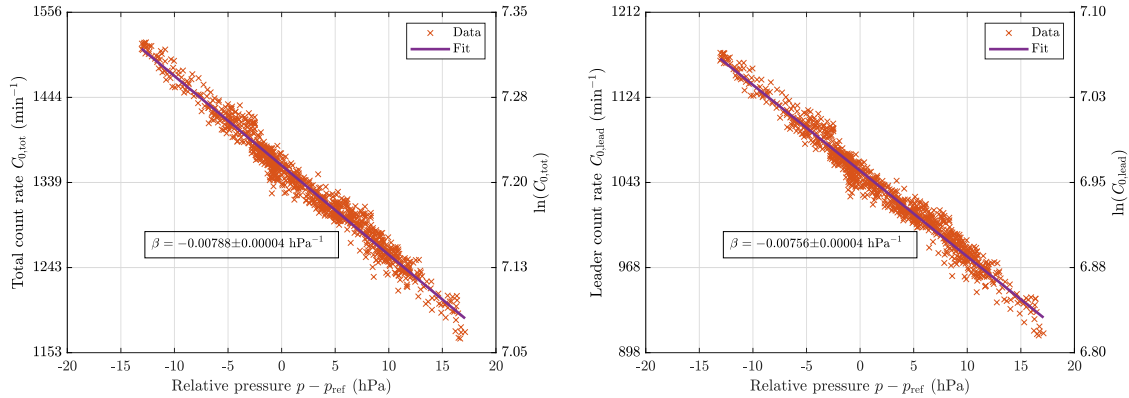


FIGURE 19. Determination of the barometric correction coefficient β including the 95% confidence interval for the minutely total count rate C_{tot} (left) and the minutely leader count rate C_{lead} (right), averaged over one hour intervals, for DOMC data from October and November 2021.

The barometric correction coefficients were determined to 0.00032 hPa^{-1} and 0.00031 hPa^{-1} for the leader fraction L_{lead} and the closely related M1 fraction L_{M1} , respectively (Fig. 20). This is similar to that reported by Banglieng et al. (2020) for the leader fraction calculated according to the method by Ruffolo et al. (2016). While Ruffolo et al. (2016) corrected the leader fraction for atmospheric pressure effects, the value of the correction coefficient was not reported. The same applies to Muangha et al. (2021), who determined the leader fraction based on Ruffolo

et al. (2016). Yakum et al. (2021) calculated the leader fraction following also the approach of Ruffolo et al. (2016), but left the determination of the barometric correction coefficients for future work.

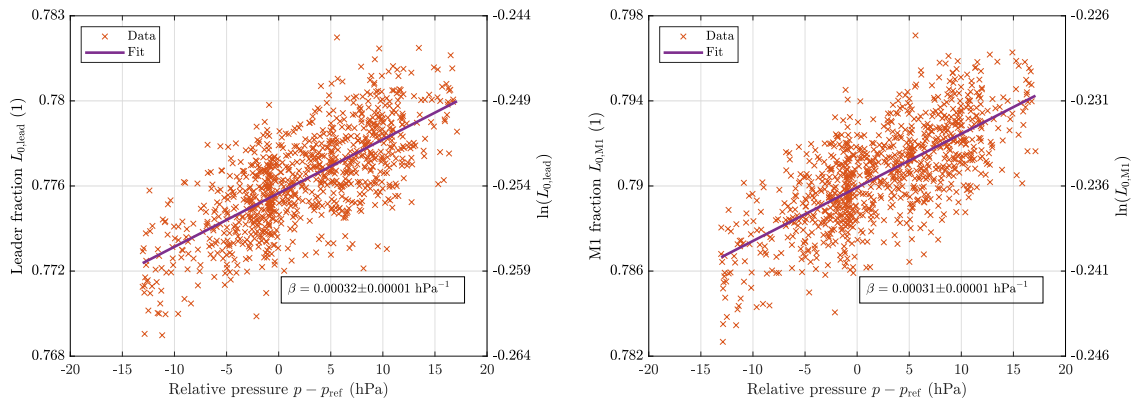


FIGURE 20. Determination of the barometric correction coefficient β including the 95% confidence interval for the leader fraction L_{lead} (left) and M1 fraction L_{M1} (right) for DOMC data from October and November 2021.

Interestingly, the dependency of the new leader fraction L_{NEW} on atmospheric pressure variations (Fig. 21) was found to be generally smaller than for the works following the approach by Ruffolo et al. (2016) for a number of NMs. The value for the barometric correction coefficient was determined to 0.00007 hPa^{-1} . Only for one of the NMs studied by Banglieng et al. (2020), a similar value for the barometric correction coefficient was found (0.00009 hPa^{-1}). The determination of the barometric correction coefficients for C_{tot} , C_{lead} , L_{lead} , L_{M1} and L_{NEW} for the DOMC NM is the fourth principal outcome of this master thesis.

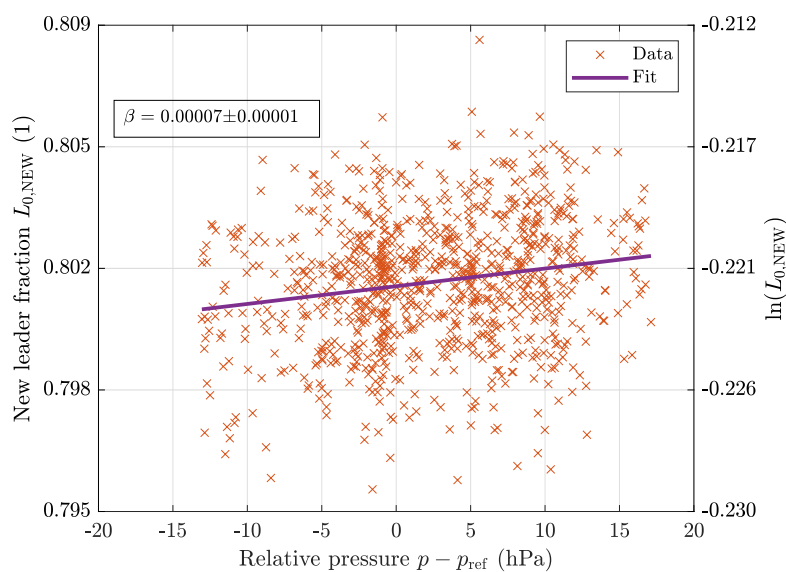


FIGURE 21. Determination of the barometric correction coefficient β including the 95% confidence interval of the new leader fraction L_{NEW} for DOMC data from October and November 2021.

4.2 Study of the GLE and Forbush decrease

In this section, the GLE 73 on the 28. October and the Forbush decrease on the 4. November 2021, respectively, are studied by means of the variables introduced in Section 3.5, that is, C_{tot} , C_{lead} , L_{lead} , L_{M1} and L_{NEW} . In particular, the leader fraction L_{lead} and M1 fraction L_{M1} , both obtained from counting pulses falling into a specific time window, are compared to the new leader fraction L_{NEW} calculated directly from the WTD, in terms of their meaningfulness and applicability as proxies for the multiplicity and the energy spectrum of incident atmospheric particles.

First, the periods associated with the GLE (28. October 00:00 – 29. October 00:00) and FD (1. November 00:00 – 12. November 00:00) are compared to the remaining data from October and November 2021, which is considered to correspond to relatively quiet periods in terms of cosmic ray intensity. Table 2 contains the mean and standard deviation of the five variables under consideration for the quiet periods (used as the background), the peak values during the GLE and FD, and the relative changes. As expected, an increase (6.4%) and a decrease (-10.4%) in the total count rate C_{tot} were observed for the GLE and FD, respectively. Noting that the background was calculated differently, Mishev et al. (2022) and Papaioannou et al. (2022) reported a slightly higher increase in count rate (7.3%) registered by DOMC during GLE 73. Compared to DOMC, the decrease in counts during the FD is stronger for some of the NM analysed by Blanco et al. (2024). However, the less pronounced drop in count rate measured by DOMC may be explained by the lower cutoff rigidity and different acceptance cones. The OULU NM, which is located in Oulu, Finland, and has a comparably low cutoff rigidity < 1GV (Larsen et al., 2023), registered a similar drop (-10.3%) in count rate during the FD as the DOMC NM (Blanco et al., 2024).

The relative changes of the leader count rate C_{lead} correspond to the expected softening and hardening of the cosmic ray spectrum during the GLE and FD, respectively, and are of similar magnitude as for the total count rate C_{tot} . The softening of the cosmic ray spectrum during the GLE 73 is confirmed by the works of Mishev et al. (2022) and Papaioannou et al. (2022). The hardening of the cosmic spectrum during the FD is consistent with Blanco et al. (2024). Using the standard deviation as a yardstick, the changes in both, the total and the leader count rates are clearly beyond the natural random variability in the underlying data.

TABLE 2. Mean and standard deviation (SD) of the pressure-corrected total count rate, leader count rate, leader fraction, M1 fraction and new leader fraction during quiet periods and the relative changes during the maxima of the GLE on the 28. October 2021 (18:00 UTC) and the Forbush decrease on the 4. November 2021 (19:00 UTC).

	Mean	SD	GLE	FD	Change GLE (%)	Change FD (%)
Total count rate C_{tot} (min^{-1})	1360	11.5	1447	1219	6.4	-10.4
Leader count rate C_{lead} (min^{-1})	1054	8.6	1122	945	6.5	-10.3
Leader fraction L_{lead} (1)	0.775	0.002	0.776	0.776	0.1	0.1
M1 fraction L_{M1} (1)	0.790	0.002	0.789	0.792	-0.1	0.3
New leader fraction L_{NEW} (1)	0.801	0.002	0.803	0.799	0.2	-0.2

The changes in the leader fraction L_{lead} and M1 fraction L_{M1} , however, are less pronounced (within one standard deviation). In addition, both L_{lead} and L_{M1} behave contrary the expected trends, that is, indicating a decrease (in case of L_{M1}) during the GLE and an increase during the FD. That increased M1/M2 ratios are sometimes observed during FD, which is contrary the spectral hardening during such events, was highlighted by Ruffolo et al. (2016).

The new leader fraction L_{NEW} on the other hand shows the expected softening (i.e. a decrease in L_{NEW}) during the GLE and hardening (i.e. an increase in L_{NEW}) during the FD. However, the changes in L_{NEW} are comparable to the standard deviation for the quiet periods. Hence, they cannot be judged statistically significant considering a standard significance level of 5%, which corresponds to approximately two standard deviations. This simplistic estimate should be complemented by a comprehensive uncertainty analysis in the future.

In the following, the behaviour of the different variables during the period of interest is analysed graphically. For this purpose, the data was aggregated for one-hour intervals, i.e. one data point represents the hourly average of the variable in question. This is a good empirical compromise between the time resolution sufficient for observations of GLE and FD and statistics needed to reflect changes in the studied quantities. Fig. 22 shows the time series of the raw and pressure-corrected total, leader and follower (i.e. the difference in the first two) count rates during October and November 2021. For the following analysis, only the pressure-corrected data is considered. Note that the gaps in the time series correspond to the periods of instrument malfunctions described in Section 3.1. Both the GLE and FD are clearly visible in the count rates. The GLE displays the expected sharp increase and decrease over a short period of time. Fig. 22 also shows the typical FD profile characterised by an abrupt drop of the count rate followed by a recovery phase lasting several days. For a more detailed discussion on the different phases of a FD, the interested reader is referred to Jordan et al. (2011) and Jämsen et al. (2007).

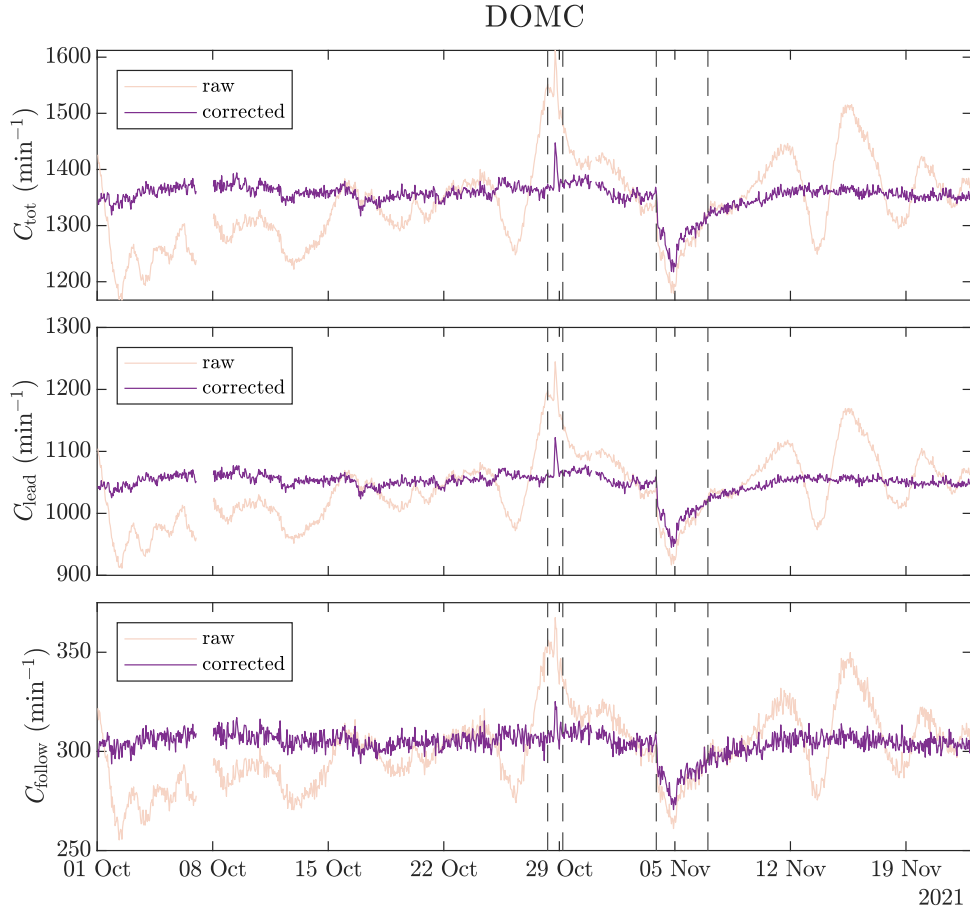


FIGURE 22. Time series of the total count rate C_{tot} (top), leader count rate C_{lead} (middle) and follower count rate C_{follow} (bottom) before (orange) and after (purple) atmospheric pressure correction for DOMC data from October and November 2021.

Fig. 23 shows the evolution of the raw and pressure-corrected L_{lead} , L_{M1} and L_{NEW} and provide for a juxtaposition with the total count rate C_{tot} . The relatively smaller dependence of L_{NEW} on atmospheric pressure variations discussed in Section 4.1 is also apparent in Fig. 23. Given the variability in the data, distinct changes during the GLE, irrespectively of the direction, are not visually recognisable from the time series of any of the three variables. This also holds when only the last couple of hours just before the GLE are used for a comparison (see Fig. 24 for a timeseries zoom).

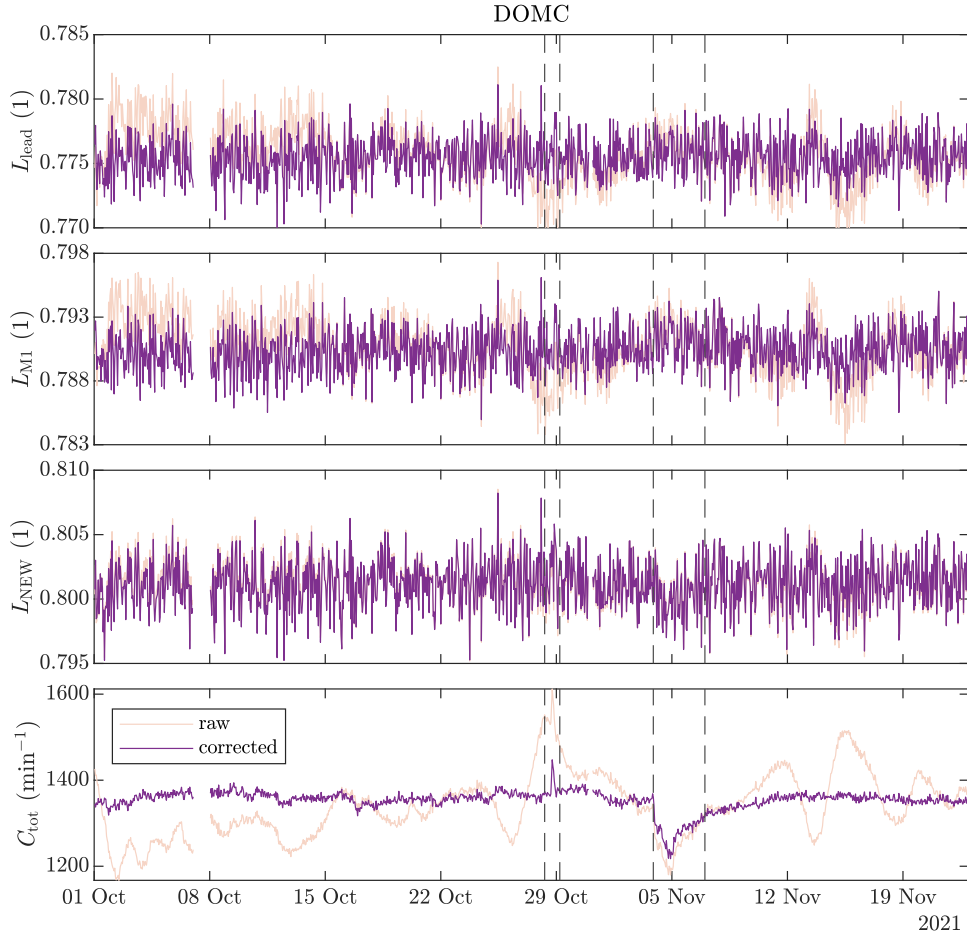


FIGURE 23. Time series of the leader fraction L_{lead} , M1 fraction L_{M1} , new leader fraction L_{NEW} and the total count rate C_{tot} (from top to bottom) before (orange) and after (purple) atmospheric pressure correction for DOMC data from October and November 2021.

With respect to the FD, both L_{lead} and L_{M1} appear in Fig. 23 to slightly increase during the FD. Again, this is contrary the hardening of the energy spectrum observed during FDs. However, when comparing the period associated with the FD to hours immediately prior the event (Fig. 25), the suggested increase of L_{lead} and L_{M1} cannot be confirmed visually. For the new leader fraction L_{NEW} calculated according to the method presented in Section 3.5, the expected decrease during the FD can be deduced graphically from both Fig. 23 and Fig. 25. This confirms the findings of the above numerical analysis based on Table 2. However, the findings for both the numerical and graphical analysis need to be taken with caution due to the variability in the underlying the data.

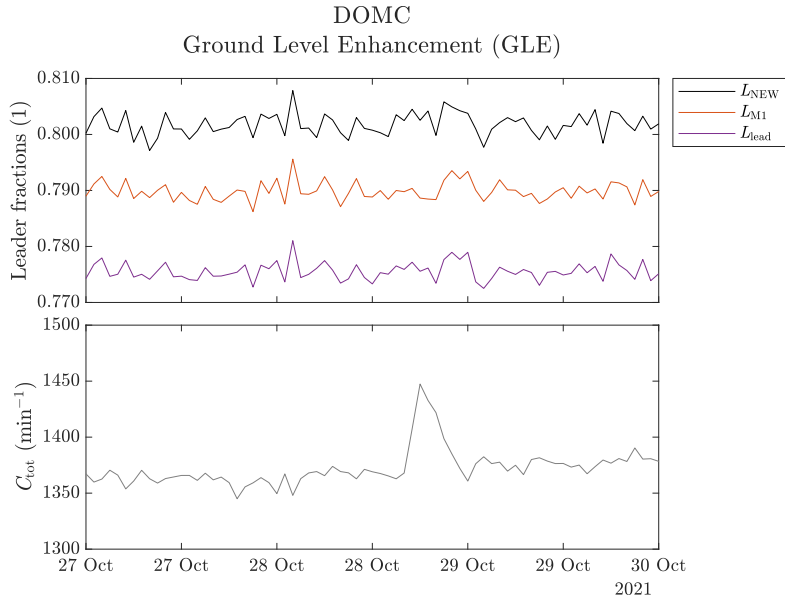


FIGURE 24. Times series close-up for the GLE 28. October 2021. Top: Different pressure-corrected measures for the leader fraction. Bottom: Minutely total count rate averaged over one hour intervals.

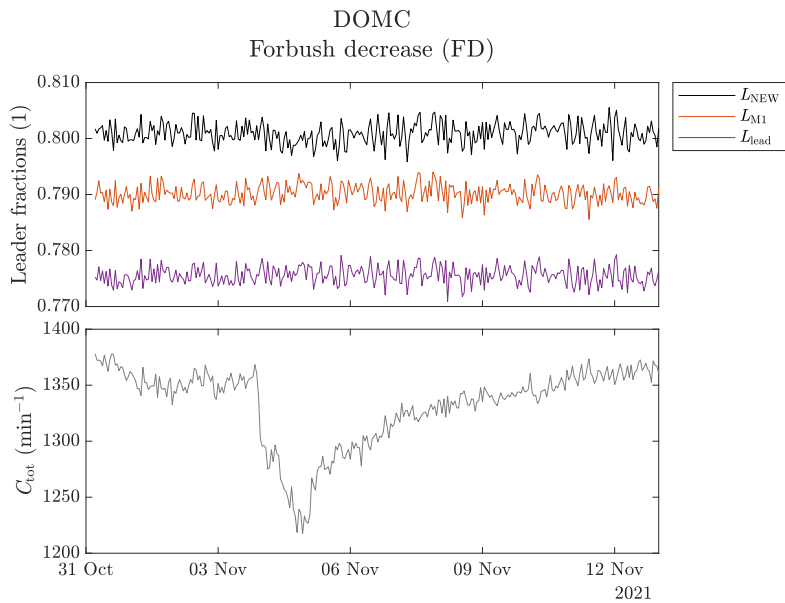


FIGURE 25. Times series close-up for the Forbush decrease 4. November 2021. Top: Different pressure-corrected measures for the leader fraction. Bottom: Minutely total count rate averaged over one hour intervals.

Next, the meaningfulness and applicability of the new leader fraction L_{NEW} as a proxy for the multiplicity and the spectral index of incident atmospheric particles is discussed on the basis of WTD. In Fig. 26, the WTD for one hour of data associated with the peak of the GLE is compared with that of a quiet period. Note that the relative pressure ΔP for both times was similar (-13.6 hPa). While the counts in the short waiting time range remains nearly constant between the two periods, there is an increase of counts in the long waiting time tail of the WTD during the GLE. This is accompanied by an increase in the new leader fraction L_{NEW} from

0.800 to 0.803 (+0.3%) (pressure-corrected values). A similar comparison for the FD is made in Fig. 27. Here, the counts in both the short waiting-time and the long-waiting time range are reduced during the FD. However, the long waiting-time tail is stronger affected by the reduction, leading to a decrease in the new leader fraction L_{NEW} from 0.801 to 0.799 (-0.2%) (pressure-corrected values).

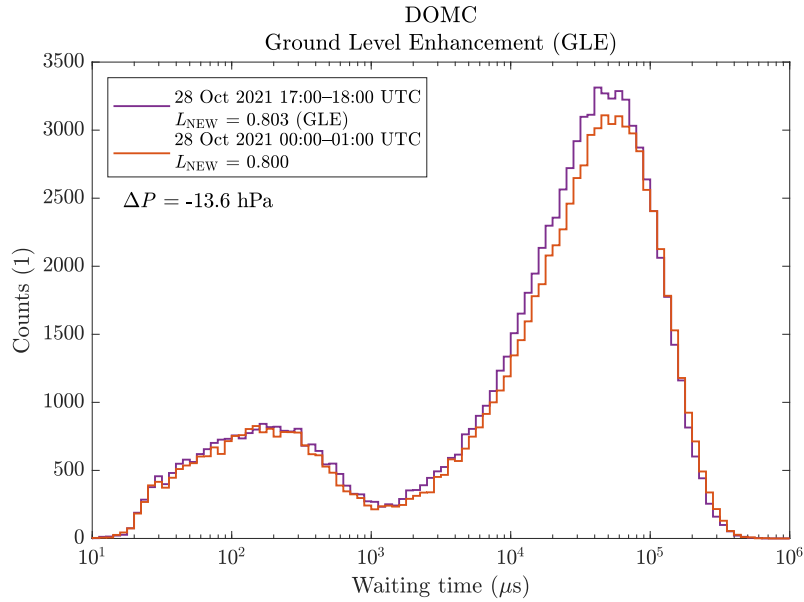


FIGURE 26. Waiting time histograms for DOMC data during the GLE 28. October 2021 and a quiet period with similar atmospheric pressure. The indicated leader fraction L_{NEW} was calculated using the new method illustrated in Fig. 18 and corrected for the atmospheric pressure.

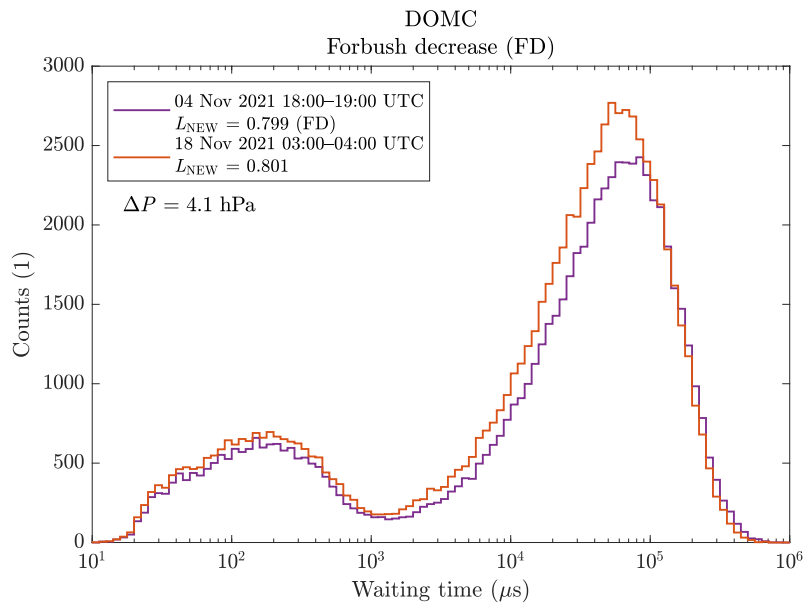


FIGURE 27. Waiting time histograms for DOMC data during the Forbush decrease 4. November 2021 and a quiet period with similar atmospheric pressure. The indicated leader fraction L_{NEW} was calculated using the new method illustrated in Fig. 18 and corrected for the atmospheric pressure.

From the numerical and graphical comparison of the different proxies for the multiplicity and the energy spectrum of incident atmospheric particles, the new leader fraction L_{NEW} appears to better reflect the expected trends during the analysed GLE and Forbush decrease. The change in L_{NEW} during the Forbush decrease can be deduced graphically from the time series and the WTD. With respect to the GLE, the change in L_{NEW} is apparent from the WTD but not from the time series. The changes in L_{NEW} during both the GLE and the Forbush decrease cannot be judged statistically significant considering the underlying variability. These findings constitute the fifth and last main result of this thesis.

5 CONCLUSIONS

In this thesis, two cosmic ray related phenomena, namely a GLE and a Forbush decrease, were studied on the basis of data generated by the DOMC NM during October and November 2021. The five main results are as follows:

1. There were observed spikes in the long waiting time tail of the WTD calculated from the timestamps of the Raspberry Pi micro-computer. The cause for the spikes was found to lie with the raw data from the DAQ of the DOMB and DOMC NM. If instead of the timestamp of the Raspberry Pi micro-computer the timestamp of the PIC32 microcontroller is used for calculating the waiting time between subsequent pulses, the spikes in the WTD disappear and the long waiting time tail follows the expected exponential shape.
2. A new method to calculate the leader fraction (denoted as L_{NEW}) was developed, which involves fitting an exponential model to the long waiting time tail of the WTD and assigning areas under the WTD to leader and follower counts.
3. DOMB is not a perfect bare NM. The neutrons escaping DOMC can reach the neighbouring DOMB and lead to the registration of $M > 1$ events. Possible solutions to this issue are an increased thickness of the reflector material in DOMC, and a greater spacing between the two NM.
4. The barometric correction coefficients for the total count rate C_{tot} , leader count rate C_{lead} , L_{lead} , M1 fraction L_{M1} and the new leader fraction L_{NEW} for the DOMC NM were determined.
5. From the numerical and graphical comparison of the different proxies for the multiplicity and the energy spectrum of incident atmospheric particles, the new leader fraction L_{NEW} appears to better reflect the expected trends during the analysed GLE and Forbush decrease. The change in L_{NEW} during the Forbush decrease can be deduced graphically from the time series and the WTD. With respect to the GLE, the change in L_{NEW} is apparent from the WTD but not from the time series. However, the changes in L_{NEW} during both the GLE and the Forbush decrease cannot be judged statistically significant considering the underlying variability.

The thesis findings have mainly two practical implications. Firstly, users of the data sets produced by DOMC and DOMB NMs are made aware of the differing

timestamps and are advised to use the one generated by the PIC32 microcontroller, until the issue related to the erroneous timestamp of the Raspberry Pi micro-computer has been resolved. Secondly, efforts should be made to improve the design of the DOMB in order to reduce the influence of DOMC. Possible solutions to this issue are an increased thickness of the reflector material in DOMC, and a greater spacing between the two NMs. However, a modification of the reflector size is unlikely, since this would mean a deviation from the standardised mini-NM design and would reduce the comparability with other instruments of that type. In addition, the limited space in the physics shelter at the Concordia research station may not allow for a significant increase in the spacing between DOMC and DOMB.

In addition to investigating the reason for the erroneous Raspberry Pi timestamp, the research presented in this thesis can be continued in several ways. It would be of interest to develop a more systematic method for defining the thresholds for filtering out noisy data, in order to support the expert judgement approach used in Section 3.1. Regarding the time series of L_{NEW} and other proxy variables for the multiplicity and the energy spectrum of incident atmospheric particles, an uncertainty analysis should be carried out to judge the statistical significance of the changes in the different proxy variables during the studied GLE and Forbush decrease. Since, due to the variability underlying the data, the meaningfulness of the studied proxy variables has been particularly difficult to judge in connection with the GLE, it would be interesting to carry out a similar analysis for a future stronger GLE. Lastly, a variation of the new method to calculate the leader fraction could be tested which involves the separation of the two populations belonging to the short and long waiting time range of the count-based WTD (Fig. 15) and assigning these to follower counts and leader counts, respectively.

REFERENCES

- Aharonian, F., Bykov, A., Parizot, E., Ptuskin, V., & Watson, A. (2012). Cosmic rays in galactic and extragalactic magnetic fields. *Space Science Reviews*, 166, 97–132.
- Aran, A., Agueda, N., Afanasiev, A., & Sanahuja, B. (2018). *Charged particle transport in the interplanetary medium*, 63–78. Springer International Publishing.
- Balabin, Y. V., Gvozdevsk, B., Maurice, E., Vashenyuk, E., & Dzhappuev, D. (2011). Fine structure of neutron multiplicity on neutron monitors. *Astrophysics and Space Sciences Transactions*, 7(3), 283–286.
- Banglieng, C., Janthaloet, H., Ruffolo, D., Sáiz, A., Mitthumsiri, W., Muangha, P., Evenson, P., Nutaro, T., Pyle, R., Seunarine, S., Madsen, J., Mangeard, S., & Macatangay, R. (2020). Tracking cosmic-ray spectral variation during 2007–2018 using neutron monitor time-delay measurements. *The Astrophysical Journal*, 890(1), 21.
- Bazilevskaya, G., Krainev, M., & Makhmutov, V. (2000). Effects of cosmic rays on the earth's environment. *Journal of Atmospheric and Solar-Terrestrial Physics*, 62(17-18), 1577–1586.
- Bazilevskaya, G. A., Cliver, E. W., Kovaltsov, G. A., Ling, A. G., Shea, M., Smart, D., & Usoskin, I. G. (2014). Solar cycle in the heliosphere and cosmic rays. *Space Science Reviews*, 186, 409–435.
- Beck, P., Latocha, M., Rollet, S., & Stehno, G. (2005). Tepec reference measurements at aircraft altitudes during a solar storm. *Advances in Space Research*, 36(9), 1627–1633.
- Béland, J., & Small, K. (2005). Space weather effects on power transmission systems: The cases of hydro-québec and transpower new zealand ltd. *Effects of space weather on technology infrastructure*, 287–299.
- Bieber, J., Clem, J., Duldig, M., Evenson, P., Humble, J., & Pyle, R. (2004). Latitude survey observations of neutron monitor multiplicity. *Journal of Geophysical Research: Space Physics*, 109(A12).
- Blanco, J. J., Ayuso, S., Regadío, A., López-Comazzi, A., García-Tejedor, J. I., García-Población, Ó., & Contreras, C. L. G. (2024). Evolution of the cosmic ray spectrum during a forrush decrease. *Advances in Space Research*.
- Boteler, D. (2021). Modeling geomagnetic interference on railway signaling track circuits. *Space Weather*, 19(1), e2020SW002609.

- Bütikofer, R. (2018). Ground-based measurements of energetic particles by neutron monitors. *Solar Particle Radiation Storms Forecasting and Analysis: The HESPERIA HORIZON 2020 Project and Beyond*, 95–111.
- Bütikofer, R., Flückiger, E., Desorgher, L., & Moser, M. (2008). The extreme solar cosmic ray particle event on 20 January 2005 and its influence on the radiation dose rate at aircraft altitude. *Science of the total environment*, 391(2-3), 177–183.
- Cane, H., Richardson, I., & Von Roseninge, T. (1993). Cosmic ray decreases and particle acceleration in 1978-1982 and the associated solar wind structures. *Journal of Geophysical Research: Space Physics*, 98(A8), 13295–13302.
- Cannon, P., Angling, M., Barclay, L., Curry, C., Dyer, C., Edwards, R., Greene, G., Hapgood, M., Horne, R., Jackson, D., Mitchell, C., Owen, J., Richards, A., Rogers, C., Ryden, K., Saunders, S., Sweeting, M., Tanner, R., Thomson, A., & Underwood, C. (2013). *Extreme space weather: impacts on engineered systems and infrastructure* (Tech. Rep.). Prince Philip House 3 Carlton House Terrace London SW1Y 5DG: Royal Academy of Engineering.
- Carmichael, H., Bercovitch, M., Shea, M., Magidin, M., & Peterson, R. (1968). Attenuation of neutron monitor radiation in the atmosphere. *Canadian journal of physics*, 46(10), S1006–S1013.
- Chaiwongkhot, K., Ruffolo, D., Yamwong, W., Prabket, J., Mangeard, P.-S., Sáiz, A., Mitthumsiri, W., Banglieng, C., Kittiya, E., Nuntiyakul, W., Tippawan, U., Jitpukdee, M., & Aukkaravittayapun, S. (2021). Measurement and simulation of the neutron propagation time distribution inside a neutron monitor. *Astroparticle Physics*, 132, 102617.
- Chukwudi, O. K., Ajisafe, A. S., & James, T. (2022). Effect of some solar energetic events on cosmic ray (cr) ground level enhancement (gle). *International Journal of Astrophysics and Space Science*, 8(1), 1–10.
- Cooke, D., Humble, J., Shea, M., Smart, D., Lund, N., Rasmussen, I., Byrnak, B., Goret, P., & Petrou, N. (1991). On cosmic-ray cut-off terminology. *Il Nuovo Cimento C*, 14, 213–234.
- Dyer, C., Hands, A., Lei, F., Truscott, P., Ryden, K. A., Morris, P., Getley, I., Bennett, L., Bennett, B., & Lewis, B. (2009). Advances in measuring and modeling the atmospheric radiation environment. *IEEE Transactions on Nuclear Science*, 56(6), 3415–3422.
- Dyer, C., Lei, F., Clucas, S., Smart, D., & Shea, M. (2003). Calculations and observations of solar particle enhancements to the radiation environment at aircraft altitudes. *Advances in Space Research*, 32(1), 81–93.
- Dyer, C., Lei, F., Hands, A., & Truscott, P. (2007). Solar particle events in the qinetiq atmospheric radiation model. *IEEE Transactions on Nuclear Science*, 54(4), 1071–1075.

- E, B., & RolfFlückiger. (2011). Radiation doses along selected flight profiles during two extreme solar cosmic ray events. *Astrophysics and Space Sciences Transactions ASTRA*, 7(2), 105–109.
- Firoz, K., Cho, K.-S., Hwang, J., Phani Kumar, D., Lee, J., Oh, S., Kaushik, S. C., Kudela, K., Rybanský, M., & Dorman, L. I. (2010). Characteristics of ground-level enhancement–associated solar flares, coronal mass ejections, and solar energetic particles. *Journal of Geophysical Research: Space Physics*, 115(A9).
- Firoz, K., Moon, Y.-J., Cho, K.-S., Hwang, J., Park, Y., Kudela, K., & Dorman, L. (2011). On the relationship between ground level enhancement and solar flare. *Journal of Geophysical Research: Space Physics*, 116(A4).
- Forbush, S. E. (1937). On the effects in cosmic-ray intensity observed during the recent magnetic storm. *Physical Review*, 51(12), 1108.
- Gerontidou, M., Katzourakis, N., Mavromichalaki, H., Yanke, V., & Eroshenko, E. (2021). World grid of cosmic ray vertical cut-off rigidity for the last decade. *Advances in Space Research*, 67(7), 2231–2240.
- Gopalswamy, N., Xie, H., Yashiro, S., Akiyama, S., Mäkelä, P., & Usoskin, I. (2012). Properties of ground level enhancement events and the associated solar eruptions during solar cycle 23. *Space Science Reviews*, 171, 23–60.
- Gopalswamy, N., Yashiro, S., Michałek, G., Kaiser, M., Howard, R., Reames, D., Leske, R., & Von Roseninge, T. (2002). Interacting coronal mass ejections and solar energetic particles. *The Astrophysical Journal*, 572(1), L103.
- Hapgood, M., Angling, M. J., Attrill, G., Bisi, M., Cannon, P. S., Dyer, C., Eastwood, J. P., Elvidge, S., Gibbs, M., Harrison, R. A., Hord, C., Horne, R. B., Jackson, D. R., Jones, B., Machin, S., Mitchell, C. N., Preston, J., Rees, J., Rogers, N. C., ... Willis, M. (2021). Development of space weather reasonable worst-case scenarios for the uk national risk assessment. *Space Weather*, 19(4). doi: <https://doi.org/10.1029/2020SW002593>
- Hatton, C. (1971). The neutron monitor. *Progress in elementary particle and cosmic ray physics*, 1–100.
- Haungs, A., Blumer, J., Fuchs, B., Kang, D., Schoo, S., Wochele, D., Wochele, J., Apel, W., Arteaga-Velázquez, J., Bekk, K., Bertaina, M., Bozdog, H., Brancus, I. M., Cantoni, E., Chiavassa, A., Cossavella, F., Daumiller, K., de Souza, V., Di Pierro, F., ... Zabierowski, J. (2015). Kcdc—the cascade cosmic-ray data centre. In *Journal of physics: Conference series* (Vol. 632, p. 012011). doi: 10.1088/1742-6596/632/1/012011
- Heber, B., Agueda, N., Bütikofer, R., Galsdorf, D., Herbst, K., Köhl, P., Labrenz, J., & Vainio, R. (2018). Inversion methodology of ground level enhancements. *Solar Particle Radiation Storms Forecasting and Analysis*, 444, 179–199.
- Hughes, E., Marsden, P., Brooke, G., Meyer, M., & Wolfendale, A. (1964). Neu-

- tron production by cosmic ray protons in lead. *Proceedings of the Physical Society*, 83(2), 239.
- Iles, R., Jones, J., Taylor, G., Blake, J., Bentley, R., Hunter, R., Harra, L., & Coates, A. (2004). Effect of solar energetic particle (sep) events on the radiation exposure levels to aircraft passengers and crew: Case study of 14 July 2000 sep event. *Journal of Geophysical Research: Space Physics*, 109(A11).
- Jämsen, T., Usoskin, I. G., Rähkä, T., Sarkamo, J., & Kovaltsov, G. (2007). Case study of forrush decreases: Energy dependence of the recovery. *Advances in Space Research*, 40(3), 342–347.
- Jiggins, P., Chavy-Macdonald, M.-A., Santin, G., Menicucci, A., Evans, H., & Hilgers, A. (2014). The magnitude and effects of extreme solar particle events. *Journal of Space Weather and Space Climate*, 4, A20.
- Jordan, A. P., Spence, H. E., Blake, J., & Shaul, D. (2011). Revisiting two-step forrush decreases. *Journal of Geophysical Research: Space Physics*, 116(A11).
- Kahler, S. (1987). Coronal mass ejections. *Reviews of Geophysics*, 25(3), 663–675.
- Knoll, G. F. (2010). *Radiation detection and measurement*. John Wiley & Sons.
- Lantos, P., & Fuller, N. (2003). History of the solar particle event radiation doses on-board aeroplanes using a semi-empirical model and concorde measurements. *Radiation Protection Dosimetry*, 104(3), 199–210.
- Larsen, N., Mishev, A., & Usoskin, I. (2023). A new open-source geomagneto-sphere propagation tool (otso) and its applications. *Journal of Geophysical Research: Space Physics*, 128(3), e2022JA031061.
- Malandraki, O. E., & Crosby, N. B. (2018). Solar energetic particles and space weather: Science and applications. *Solar particle radiation storms forecasting and analysis: the HESPERIA HORIZON 2020 project and beyond*, 1–26.
- Mangeard, P.-S., Ruffolo, D., Sáiz, A., Nuntiyakul, W., Bieber, J., Clem, J., Evenson, P., Pyle, R., Duldig, M., & Humble, J. (2016). Dependence of the neutron monitor count rate and time delay distribution on the rigidity spectrum of primary cosmic rays. *Journal of Geophysical Research: Space Physics*, 121(12), 11–620.
- Matthiä, D., Heber, B., Reitz, G., Meier, M., Sihver, L., Berger, T., & Herbst, K. (2009). Temporal and spatial evolution of the solar energetic particle event on 20 January 2005 and resulting radiation doses in aviation. *Journal of Geophysical Research: Space Physics*, 114(A8).
- Matthiä, D., Heber, B., Reitz, G., Sihver, L., Berger, T., & Meier, M. (2009). The ground level event 70 on December 13th, 2006 and related effective doses at aviation altitudes. *Radiation Protection Dosimetry*, 136(4), 304–310.
- Medina, J., Blanco, J. J., García, O., Gómez-Herrero, R., Catalán, E. J., García, I.,

- Hidalgo, M. A., Meziat, D., Prieto, M., Rodríguez-Pacheco, J., & Sánchez, S. (2013). Castilla-la mancha neutron monitor. *Nuclear Instruments and Methods in Physics Research Section A: Accelerators, Spectrometers, Detectors and Associated Equipment*, 727, 97–103.
- Miroshnichenko, L. I. (2018). Retrospective analysis of gles and estimates of radiation risks. *Journal of Space Weather and Space Climate*, 8, A52.
- Mishev, A., & Poluianov, S. (2021). About the altitude profile of the atmospheric cut-off of cosmic rays: new revised assessment. *Solar Physics*, 296(8), 129.
- Mishev, A. L., Kocharov, L. G., Koldobskiy, S. A., Larsen, N., Riihonen, E., Vainio, R., & Usoskin, I. G. (2022). High-resolution spectral and anisotropy characteristics of solar protons during the gle n \square 73 on 28 october 2021 derived with neutron-monitor data analysis. *Solar Physics*, 297(7), 88.
- Muangha, P., Ruffolo, D., Sáiz, A., Banglieng, C., Evenson, P., Seunarine, S., Oh, S., Jung, J., Duldig, M., & Humble, J. (2021, July). Time-delay measurements from antarctic neutron monitor stations indicate weak spectral changes during 27-day variations. In *37th international cosmic ray conference (icrc 2021)*. Berlin, Germany.
- Papaioannou, A., Kouloumvakos, A., Mishev, A., Vainio, R., Usoskin, I., Herbst, K., Rouillard, A., Anastasiadis, A., Gieseler, J., Wimmer-Schweingruber, R., & Köhl, P. (2022). The first ground-level enhancement of solar cycle 25 on 28 october 2021. *Astronomy & Astrophysics*, 660, L5.
- Poluianov, S., & Batalla, O. (2022). Cosmic-ray atmospheric cutoff energies of polar neutron monitors. *Advances in Space Research*, 70(9), 2610–2617.
- Poluianov, S., Usoskin, I., Mishev, A., Moraal, H., Kruger, H., Casasanta, G., Traversi, R., & Udisti, R. (2015). Mini neutron monitors at concordia research station, central antarctica. *Journal of Astronomy and Space Sciences*, 32(4), 281–287. doi: 10.5140/JASS.2015.32.4.281
- Poluianov, S., Usoskin, I., Mishev, A., Shea, M., & Smart, D. (2017). Gle and sub-gle redefinition in the light of high-altitude polar neutron monitors. *Solar Physics*, 292(11), 176.
- Prof. Strauss, D. T. (2024, March). private communication.
- Rao, U. R., McCracken, K., & Venkatesan, D. (1963). Asymptotic cones of acceptance and their use in the study of the daily variation of cosmic radiation. *Journal of Geophysical Research*, 68(2), 345–369.
- Ruffolo, D., Saiz, A., Kamyran, N., Nutaro, T., Sumran, S., Chaiwattana, C., Gasiprong, N., Channok, C., Rujiwarodom, M., Tooprakai, P., ASAVAPIB-HOP, B., Bieber, W., Clem, J. M., Evenson, P., & Munakata, K. (2011). Neutron time delay analysis for the princess sirindhorn neutron monitor at doi inthanon, thailand. In *International cosmic ray conference* (Vol. 11, p. 264).
- Ruffolo, D., Saiz, A., Mangeard, P.-S., Kamyran, N., Muangha, P., Nutaro, T., Sum-

- ran, S., Chaiwattana, C., Gasiprong, N., Channok, C., Wuttiya, C., Rujiwarodom, M., Tooprakai, P., Asavapibhop, J., Bieber, W., Clem, J., Evenson, P., & Munakata, K. (2016). Monitoring short-term cosmic-ray spectral variations using neutron monitor time-delay measurements. *The Astrophysical Journal*, *817*(1), 38.
- Shea, M., & Smart, D. (2012). Space weather and the ground-level solar proton events of the 23rd solar cycle. *Space science reviews*, *171*(1-4), 161–188.
- Similä, M., Usoskin, I., Poluianov, S., Mishev, A., Kovaltsov, G. A., & Strauss, D. T. (2021). High-altitude polar nm with the new daq system as a tool to study details of the cosmic-ray induced nucleonic cascade. *Journal of Geophysical Research: Space Physics*, *126*(4), e2020JA028959.
- Simpson, J. (1957). *Cosmic radiation intensity monitor, annals igy, iv, 351*. Pergamon Press, London.
- Smart, D., & Shea, M. (2009). Fifty years of progress in geomagnetic cutoff rigidity determinations. *Advances in Space Research*, *44*(10), 1107–1123.
- Strauss, D. T., & Diedericks, C. (2018, August). Mini-neutron monitor handbook and guide [Computer software manual]. (Available at <https://example.com/manual.pdf>)
- Strauss, D. T., Poluianov, S., van der Merwe, C., Krüger, H., Diedericks, C., Krüger, H., Usoskin, I., Heber, B., Nndanganeni, R., Blanco-Ávalos, J., García-Tejedor, I., Herbst, K., Caballero-Lopez, R., Moloto, K., Lara, A., Walter, M., Mezgebe Giday, N., & Traversi, R. (2020). The mini-neutron monitor: a new approach in neutron monitor design. *Journal of Space Weather and Space Climate*, *10*, 39.
- Strauss, R., Giday, N. M., Seba, E. B., Chekole, D. A., Garuma, G. F., Kassa, B. H., Dugassa, T., & Diedericks, C. (2022). First results from the entoto neutron monitor: Quantifying the waiting time distribution. *Advances in Space Research*.
- The MathWorks Inc. (2023). MATLAB version 23.2.0.2365128 (R2023b) [Computer software manual]. Natick, Massachusetts, United States. Retrieved from <https://www.mathworks.com>
- Wheatland, M. (2003). The coronal mass ejection waiting-time distribution. *Solar Physics*, *214*, 361–373.
- Wheatland, M., & Litvinenko, Y. E. (2002). Understanding solar flare waiting-time distributions. *Solar Physics*, *211*, 255–274.
- Yakum, P., Jiang, P., Chuanraksasat, P., Nuntiyakul, W., Ruffolo, D., Sáiz, A., Banglieng, C., Evenson, P., Munakata, K., Madsen, J., Soonthorntham, B., Komonjinda, S., & Macatangay, R. (2021). Preliminary analysis of neutron time-delay histograms from changvan latitude surveys. In *Journal of physics: Conference series* (Vol. 1719, p. 012006).